Decoupled Potential Integral Equation for Electromagnetic Scattering From Arbitrarily Shaped Dielectric Objects

L. Baumann, *Student Member, IEEE*, H. M. Aktulga, C. Macon, *Senior Member, IEEE*, and B. Shanker, *Fellow, IEEE*

Abstract—Recently, integral equation formulations that use potentials as opposed to fields as unknown quantities have been developed for scattering from dielectric objects. It has been shown that these formulations can be construed so that they are wellconditioned across a broad frequency spectrum, a result that has been theoretically proven for spherical systems. Unfortunately, to date, this formulation has not been implemented on practical discretizations of objects. This is the goal of this paper. Specifically, we present a well-conditioned and well-tested Decoupled Potential Integral Equation (DPIE) formulation and all the necessary implementation details for electromagnetic scattering from homogeneous, dielectric, arbitrarily shaped objects. The resulting decoupled systems do not suffer from low frequency breakdown. Results that demonstrate these properties are presented for a number of different dielectric targets. Furthermore, in order to fully validate each of the two integral equation for the potentials, we develop analytical solutions for spherical systems.

Index Terms—DPIE, Scalar Potential Integral Equation (SPIE), Vector Potential Integral Equation (VPIE), Poggio-Miller-Chang-Harrington-Wu-Tsai (PMCHWT), Müller

I. INTRODUCTION

THE analysis of scattering from non-canonical dielectric objects was first addressed five decades ago. The usual surface integral equation framework relies on equivalence theorems to define both the exterior and interior equivalent problems and then reduces the number of equations by imposing constraints derived from boundary conditions. The most popular equations in this vein are the Poggio-Miller-Chang-Harrington-Wu-Tsai (PMCHWT) [1] and Müller [2] formulations, but it should be noted that several other formulations are possible and have been investigated in the past. These include a single integral equation [3, 4] as well as various combinations of surface equivalence theorems; see [5], [6], and references therein for some combinations. The necessity of analyzing composite objects has driven vast advances in the machinery and techniques necessary to accurately compute scattering. Expressly, the primary challenges include dense mesh breakdown [7], low frequency breakdown [8, 9], and topology breakdown [10]. All of these occur when representing and measuring

Manuscript received March XX, 2021; revised September XX, 2021.

these integral equations on tessellated representations of the scatter and arise due to either catastrophic cancellation or bad constraints/scaling of the integral equations. A consequence of these breakdowns is that the resulting discrete systems are ill-conditioned and poorly convergent. As a result, there has been a concerted effort to develop well-conditioned formulations in both the electromagnetics and applied mathematics communities [11–15] for a while.

Indeed, early work recognizing these challenges and efforts toward amelioration date back four decades [8, 16–18] with the introduction of loop-star and loop-tree decomposition. Development of preconditioners, formulations, as well as appropriate basis sets to effect these numerically has been a topic of intense research over the past decade [19]. By and large, these methods rely on proper representation of traces or twisted traces of the fields on the surface. More recently, research has focused on alternative formulations which will be the emphasis of the remainder of this paper.

A common thread to overcome some of the bottleneck of the classical integral equations has been the reliance on using either Debye potentials [20, 21], DPIE [22-25], Decoupled Field Integral Equation (DFIE) [26], or Dirac formulations [27]. In what follows, we focus on the DPIE for dielectric objects which amounts to two sub-formulations, the Scalar Potential Integral Equation (SPIE) and Vector Potential Integral Equation (VPIE). In effect, this is a solution to the transmission problem posed in terms of potentials such that boundary conditions on fields are strictly enforced. It has been shown that the DPIE is more robust to breakdowns associated with low frequency, mesh discretization, and topology [24]. As is usually the case, this approach was first developed to analyze scattering from Perfect Electrical Conductors (PECs) [22-24]. A corrected Nyström's method implementation was presented in [28] and a time domain potential based integral equation solvers [29, 30] currently exist. As an aside, it can be shown that [23], while based on potential, is akin to an Augmented Electric Field Integral Equation (A-EFIE) [31]. As is to be expected, developing equations for analysis of scattering from dielectric objects is more complicated. It has its genesis in [24, 25, 32]. It is well-conditioned and not susceptible to nonuniqueness due to resonances (under assumptions on constitutive parameters [26, 27]) nor breakdown due to either low frequencies or topology. All these features were demonstrated using either analytical basis sets on spheres or Nyström's method on canonical geometries. The analysis using potentials

L. Baumann and B. Shanker are with the Department of Electrical and Computer Engineering, Michigan State University, East Lansing, MI, 48824

H. M. Aktulga is with the Department of Computer Science, Michigan State University, East Lansing, MI, 48824 USA.

C. Macon is with the Air Force Research Laboratory, Wright-Patterson AFB, OH USA.

was first presented by [24] who then continued their work by developing the DFIE formulation for dielectrics using an indirect method [26]. It has been noted that the DFIE is non-unique for certain pairs of constitutive parameters when loss is present. The formulations presented in this paper are presumed to have the same problem and only lossless materials are considered. A more robust formulation has recently been introduced that has similar properties for a wider range of constitutive properties [27]. Since the publication of [24] and [32], there has not been a transition to scattering analysis on tessellated geometries. The complexity of the operators is deceptively daunting, but in what follows, we present details necessary to implement the DPIE on tessellated surfaces and show that the properties demonstrated using analytical basis sets are preserved. In addition, we present an analytical solution to the DPIE that makes it possible to investigate other formulation variants.

The rest of this paper is organized as follows: The problem statement and notation are presented in Section II. A brief overview of the representation and formulation occur in Sections III-IV. The implementation details are provided in Section V with a plethora of accompanying results in Section VI that validate the properties. Appendices provide details of analytic representation as well as integration on tessellated surfaces.

II. Preliminaries

A. Problem Statement

Consider a homogeneous dielectric body occupying a volume Ω_2 that is immersed in a homogeneous background Ω_1 . The boundary of the scatterer is defined by a two-dimensional manifold $\partial\Omega$ embedded in \mathbb{R}^3 with a unique outward pointing normal $\hat{\mathbf{n}}$ (r) that is defined for all points $\mathbf{r} \in \partial \Omega$ except a finite number of geometrically singular points (e.g., corners, tips, and edges). For convenience, we will use $\hat{\mathbf{n}}_{n}(\mathbf{r}) =$ $\varepsilon_p \hat{\mathbf{n}}$ (\mathbf{r}) to denote normal unit vectors that point into Ω_p , with $p \in \{1,2\}$ and $\varepsilon_p = (-1)^{p-1}$. Likewise, quantities associated with domain Ω_p will be denoted with the subscript p. The constitutive parameters of each region are described by the relative permittivity ϵ_{rp} and relative permeability μ_{rp} . Other defined regional quantities include wavenumber $\kappa_p = \omega \sqrt{\mu_p \epsilon_p}$ and refractive index $n_p = \sqrt{\mu_{rp}\epsilon_{rp}}$.

We seek to compute the scattered fields $\{\mathbf{E}_{n}^{s}(\mathbf{r}), \mathbf{H}_{n}^{s}(\mathbf{r})\}$ due to a plane wave given by $\left\{ m{\kappa}_{1}, \mathbf{E}_{1}^{i}\left(\mathbf{r}\right), \mathbf{H}_{1}^{i}\left(\mathbf{r}\right) \right\}$ that is incident on the dielectric scattering body with wavenumber and direction κ_1 . Total, incident, and scattered quantities will be denoted with superscript t, i, and s, respectively. The total fields $\{\mathbf{E}_{p}^{t}(\mathbf{r}), \mathbf{H}_{p}^{t}(\mathbf{r})\}$ in each region Ω_{p} obey the boundary conditions on $\partial\Omega$ and the scattered fields $\{\mathbf{E}_{1}^{s}(\mathbf{r}), \mathbf{H}_{1}^{s}(\mathbf{r})\}$ in the background Ω_1 obey the radiation boundary condition. In what follows, we assume a time dependence of $\exp(j\omega t)$ and suppress it throughout. Next, we present the notation that is used in the paper followed by a brief summary of the DPIE formulation.

B. Notation

As is usually done, spatial location is denoted by r; under convolution with the Green's function, source quantities will be denoted with a prime as in \mathbf{r}' . When unambiguous, we will omit writing the dependence on spatial locations. Operators will be denoted with upper case calligraphy as in \mathcal{O} . Likewise, we will have matrices of operators acting on a vector of functions. To facilitate these actions, we will adopt matrix notation and use o to denote the action of an operator (or a block operator matrix) on a function (or vector of functions). We will denote a matrix using underlined calligraphy, as in \mathcal{M} . Finally, we define a single-layer potential operator that can operate on either scalars or vectors as

$$S_{p} \circ \begin{pmatrix} \mathbf{x} \\ x \end{pmatrix}^{T} = \int G_{p}(\mathbf{r}, \mathbf{r}') \begin{pmatrix} \mathbf{x}(\mathbf{r}') \\ x(\mathbf{r}') \end{pmatrix}^{T} dS'$$
 (1)

where

$$G_p = \frac{\exp(-j\kappa_p |\mathbf{r} - \mathbf{r}'|)}{4\pi |\mathbf{r} - \mathbf{r}'|}$$
(2)

denotes the Green's function for the scalar Helmholtz equation in a homogeneous region p with wavenumber κ_p . All other integral operators used throughout the paper and defined in Appendix A are with respect to the single-layer potential operator.

III. REPRESENTATION VIA POTENTIALS

The crux of the DPIE relies on developing an integral equation for each of the electric scalar and magnetic vector potentials. In this paper, the representation for the potentials follows that in [32]. For the SPIE, the scaling on the unknowns is modified to more closely match how the VPIE scales its unknowns. For the VPIE, there are two changes. The first change is a modification to the unknowns (changing whether certain unknowns are traces or twisted traces) such that the piecewise vector basis functions are div-conforming rather than curl-conforming as seen in Section V-A2. The second is the relationship between divergence of the magnetic vector potential in two regions; in this paper we have strictly enforced the Lorenz gauge. For the sake of completeness and to introduce a unifying formulation for the two integral equations, we review both using the notation developed earlier.

A. SPIE

The SPIE relies on two surface quantities, the electric scalar potential and its normal derivative. A surface integral representation of the scattered electric scalar potential in region p, derived from the Helmholtz equation and Green's identity, can be succinctly written as

$$\phi_p^s = \mathcal{D}_p \circ \alpha_p^t - \mathcal{S}_p \circ \beta_p^t \tag{3}$$

with

$$\alpha_n = \phi_n \tag{4a}$$

$$\alpha_p = \phi_p \tag{4a}$$
$$\beta_p = \hat{\mathbf{n}}_p \cdot \nabla \phi_p. \tag{4b}$$

B. VPIE

The VPIE is a little more complicated. Four unknown quantities are necessary to recover the magentic vector potential [32]. They are the twisted trace of the curl, the trace, the normal component, and divergence of the magnetic vector potential. A surface integral representation of the scattered magnetic vector potential in region p, again derived from the Helmholtz equation and the vector analog to Green's identity, can be succinctly written as

$$\mathbf{A}_{p}^{s} = -\mathcal{S}_{p} \circ (\hat{\mathbf{n}}_{p} \times \mathbf{a}_{p}^{t}) + \nabla \times \mathcal{S}_{p} \circ \mathbf{b}_{p}^{t} - \nabla \mathcal{S}_{p} \circ \gamma_{p}^{t} - \mathcal{S}_{p} \circ \sigma_{p}^{t}.$$
(5)

with

$$\mathbf{a}_{p} = \hat{\mathbf{n}}_{p} \times \hat{\mathbf{n}}_{p} \times \nabla \times \mathbf{A}_{p} \tag{6a}$$

$$\mathbf{b}_{n} = \hat{\mathbf{n}}_{n} \times \mathbf{A}_{n} \tag{6b}$$

$$\gamma_p = \hat{\mathbf{n}}_p \cdot \mathbf{A}_p \tag{6c}$$

$$\sigma_p = \nabla \cdot \mathbf{A}_p. \tag{6d}$$

IV. REQUISITE INTEGRAL EQUATIONS

To construct the SPIE and VPIE formulations we start by examining the integral equations for each region individually, viz,

$$\begin{pmatrix}
\alpha_{p}^{t} \\
\beta_{p}^{t}
\end{pmatrix} = \begin{pmatrix}
\alpha_{p}^{i} \\
\beta_{p}^{i}
\end{pmatrix} + \begin{pmatrix}
\mathcal{D}_{p} & -\mathcal{S}_{p} \\
\mathcal{N}_{p} & -\mathcal{D}_{p}^{\prime}
\end{pmatrix} \circ \begin{pmatrix}
\alpha_{p}^{t} \\
\beta_{p}^{t}
\end{pmatrix} \tag{7a}$$

$$\begin{pmatrix}
\mathbf{a}_{p}^{t} \\
\mathbf{b}_{p}^{t} \\
\gamma_{p}^{t} \\
\sigma_{p}^{t}
\end{pmatrix} = \begin{pmatrix}
\mathbf{a}_{p}^{i} \\
\mathbf{b}_{p}^{i} \\
\gamma_{p}^{i} \\
\sigma_{p}^{i}
\end{pmatrix} + \begin{pmatrix}
\mathcal{K}_{p}^{t} & \kappa_{p}^{2} \mathcal{L}_{p}^{t} & 0 & -\mathcal{Q}_{p}^{1} \\
-\mathcal{J}_{p}^{2} & \mathcal{K}_{p} & -\mathcal{P}_{p}^{2} & -\mathcal{Q}_{p}^{2} \\
-\mathcal{J}_{p}^{3} & \mathcal{M}_{p}^{3} & -\mathcal{D}_{p}^{\prime} & -\mathcal{Q}_{p}^{3} \\
-\mathcal{J}_{p}^{4} & 0 & \kappa_{p}^{2} \mathcal{S}_{p} & \mathcal{D}_{p}
\end{pmatrix} \circ \begin{pmatrix}
\mathbf{a}_{p}^{t} \\
\mathbf{b}_{p}^{t} \\
\gamma_{p}^{t} \\
\sigma_{p}^{t}
\end{pmatrix} \tag{7b}$$

These operators are defined in Appendix A. For convenience, we can let the block operator matrices be denoted as \mathcal{Z}_p^{χ} and the vector of traces as $\boldsymbol{\tau}_p^{\chi}$, with $\chi \in \{S, V\}$ for either SPIE or VPIE respectively, which leads to a condensed way of writing both formulations,

$$\boldsymbol{\tau}_{p}^{t^{\chi}} = \boldsymbol{\tau}_{p}^{i^{\chi}} + \mathcal{Z}_{p}^{\chi} \circ \boldsymbol{\tau}_{p}^{t^{\chi}}. \tag{8}$$

Evaluating the left-hand side as \mathbf{r} approaches $\partial\Omega$ from within Ω_p , leads to

$$\boldsymbol{\tau}_{p}^{i^{\chi}} = \left(\mathcal{I} - \mathcal{Z}_{p}^{\chi}\right) \circ \boldsymbol{\tau}_{p}^{t^{\chi}}$$
 (9)

where \mathcal{I} is the idempotent.

Next, boundary conditions are imposed on the potentials through $\tau_p^{t^\chi}$ so as to satisfy the boundary conditions on the electric and magnetic fields. As elucidated in [32], the boundary conditions on the potentials are derived from those on electric and magnetic fields, but stricter. They can be expressed as diagonal matrices and are used to form unknown surface quantities; specifically

$$\underline{\mathcal{P}}_{1}^{\chi} \boldsymbol{\tau}_{1}^{t^{\chi}} = \underline{\mathcal{P}}_{2}^{\chi} \boldsymbol{\tau}_{2}^{t^{\chi}} = \bar{\boldsymbol{\tau}}^{t^{\chi}}. \tag{10}$$

where \mathcal{P}_p^{χ} defines a diagonal matrix that imposes the appropriate boundary conditions. For the two formulations, they are

$$\underline{\mathcal{P}}_{p}^{S} = \sqrt{\epsilon_{0}} \operatorname{diag}\left(-j\kappa_{0}, \varepsilon_{p}\epsilon_{rp}\right) \tag{11a}$$

$$\underline{\mathcal{P}}_{p}^{V} = \frac{1}{\sqrt{\mu_{0}}} \operatorname{diag}\left(\frac{1}{\mu_{rp}}, -\varepsilon_{p}j\kappa_{0}, -\varepsilon_{p}j\kappa_{0}\epsilon_{rp}, \frac{1}{\mu_{rp}\epsilon_{rp}}\right).$$
(11b)

In (11b), the boundary condition on $\sigma_p^t = \nabla \cdot \mathbf{A}_p^t$ has been corrected from [32]. The two diagonal matrices are scaled such that the unknowns in *both* formulations are of the same units.

In addition to these conditions, one can choose scale factors as detailed in [32] to obtain a better conditioned system. The resulting set of equations for both systems can be written as

$$\underline{\mathcal{P}_{p}^{\chi}}\underline{\mathcal{W}_{p}^{\chi}}\boldsymbol{\tau}_{p}^{i^{\chi}} = \underline{\mathcal{P}_{p}^{\chi}}\underline{\mathcal{W}_{p}^{\chi}}\left(\mathcal{I} - \mathcal{Z}_{p}^{\chi}\right) \circ \left(\left(\underline{\mathcal{P}_{p}^{\chi}}\right)^{-1}\bar{\boldsymbol{\tau}}_{p}^{t^{\chi}}\right) \tag{12}$$

with $\mathcal{D}_p^{\chi} \mathcal{W}_p^{\chi}$ applied to both sides to scale the system for each region. For the two formulations, the remaining matrices to be defined are

$$\underline{\mathcal{W}}_{p}^{S} = \operatorname{diag}\left(1, \frac{1}{\epsilon_{rp}}\right) \tag{13a}$$

$$\underline{\mathcal{W}}_{p}^{V} = \operatorname{diag}\left(\mu_{rp}, \epsilon_{rp}, \frac{1}{\epsilon_{rp}}, \frac{1}{\mu_{rp}}\right).$$
(13b)

There is some freedom when choosing the scale factors $\underline{\mathcal{W}}_p^S$, however, the choice can play a significant role in the behavior of the formulation. The choice given in (13a) leads to the SPIE being a second-kind integral equation that is immune to low frequency and dense mesh breakdowns.

Finally, for the purposes of uniqueness, the normal derivative of the electric scalar potential and the normal component of the magnetic vector potential have to satisfy a zero mean constraint,

$$\int \beta_p^t(\mathbf{r}') \, dS' = 0 \tag{14a}$$

$$\int \gamma_p^t(\mathbf{r}') \, dS' = 0. \tag{14b}$$

Because of the boundary conditions, if the zero-mean constraints are satisfied in either region, then they are satisfied in both regions. Implementation of these zero-mean constraints will be addressed further in Section V-C.

V. IMPLEMENTATION: ANALYTIC AND PIECEWISE BASIS SETS

Next, we discuss discretization of these operators using both analytic and piecewise triangulation basis sets. The former provides the means for validation of the resulting discrete matrix system, its convergence against analytical data, as well as end results (say Radar Cross Section (RCS) or traces on surface). Furthermore, it provides us the necessary means to explore different formulations, with regard to broadband behavior, null spaces, robustness to complex material properties, etc. The latter permits analysis of scattering from practical objects.

A. Preliminaries

The integral equations presented thus far are agnostic to the basis functions used to discretize these systems. Note, for the SPIE one needs scalar basis sets whereas for the VPIE both scalar and vector functions are needed. For ease of presentation (and implementation), we introduce some additional notation. Let the space of scalar basis functions be denoted using $\underline{\mathcal{B}}_n^s$, for $n \in [0, N_s)$. Likewise, the space of vector basis functions are denoted using $\underline{\mathcal{B}}_n^v$, for $n \in [0, N_v)$. In the above, we note that N_s and N_v are the number of scalar and vector basis functions. The number of degrees of freedom for the SPIE is $2N_s$ and that for the VPIE is $2N_v + 2N_s$. It follows that one can represent the collection of scalar basis functions of dimension $2N_s$ using $\underline{\mathcal{F}}^S = \operatorname{diag}(\underline{\mathcal{B}}^s,\underline{\mathcal{B}}^s)$, where "diag" here is used to mean a block-diagonal matrix. The space spanned by these functions is denoted using $\bar{\tau}_p^{tS} = \sum_{n=0}^{2N_s-1} \underline{\mathcal{F}}_n^S y_n^S$ where the n^{th} coefficient is denoted using y_n^S (for $n \in [0, 2N_s)$). In a similar manner, we can collect vector and scalar basis functions for discretizing the VPIE using $\underline{\mathcal{F}}^V = \mathrm{diag}\left(\underline{\mathcal{B}}^v, \underline{\mathcal{B}}^v, \underline{\mathcal{B}}^s, \underline{\mathcal{B}}^s\right)$ denoting its span using $\bar{\tau}_p^{t^V}$ and corresponding coefficients using y_n^V (for $n \in [0, 2N_v + 2N_s)$). Given these definitions, we briefly prescribe both analytical and piecewise basis sets for both the SPIE and

1) Analytic Basis Sets: For analysis on a sphere of radius a, we employ scalar and vector spherical harmonics as defined in Appendix B. As usual, we limit the number of harmonics used to represent the potentials to N_h . In the spirit of our earlier discussion, we define

$$\underline{\mathcal{B}}_{\mathbf{Y}} = \begin{pmatrix} \mathbf{Y}_0^0 & \dots & \mathbf{Y}_l^m & \dots & \mathbf{Y}_{N_h}^{N_h} \end{pmatrix}$$
 (15a)

$$\underline{\mathcal{B}}_{\mathbf{\Psi}} = \begin{pmatrix} \mathbf{\Psi}_0^0 & \dots & \mathbf{\Psi}_l^m & \dots & \mathbf{\Psi}_{N_h}^{N_h} \end{pmatrix} \tag{15b}$$

$$\underline{\mathcal{B}}_{\mathbf{\Phi}} = \left(\mathbf{\Phi}_{0}^{0} \dots \mathbf{\Phi}_{l}^{m} \dots \mathbf{\Phi}_{N_{h}}^{N_{h}}\right) \tag{15c}$$

Scalar unknowns are represented with Y_l^m and vector unknowns are represented with both Ψ_l^m and Φ_l^m

$$\underline{\mathcal{B}}^s = \underline{\mathcal{B}}_{Y} \tag{16a}$$

$$\underline{\mathcal{B}}^{v} = \begin{pmatrix} \underline{\mathcal{B}}_{\mathbf{\Psi}} & \underline{\mathcal{B}}_{\mathbf{\Phi}} \end{pmatrix} \tag{16b}$$

with $N_s = (N_h + 1)^2$ and $N_v = 2(N_h + 1)^2$.

2) Piecewise Basis Sets: For analysis on a triangular mesh with N_f flat-triangles and N_e edges, we employ pulse and Rao-Wilton-Glisson (RWG) functions defined as:

$$p_{n_f}(\mathbf{r}) = \begin{cases} 1 & \mathbf{r} \in T_{n_f} \\ 0 & \mathbf{r} \notin T_{n_f} \end{cases}$$
 (17a)

$$\mathbf{f}_{n_{e}}\left(\mathbf{r}\right) = \begin{cases} \frac{l_{n_{e}}}{2A_{n_{e}}^{\pm}} \boldsymbol{\varrho}_{n_{e}}^{\pm}\left(\mathbf{r}\right) & \mathbf{r} \in T_{n_{e}}^{\pm} \\ \mathbf{0} & \mathbf{r} \notin T_{n_{e}}^{\pm} \end{cases}$$
(17b)

where

$$\boldsymbol{\varrho}_{n_e}^{\pm}\left(\mathbf{r}\right) = \begin{cases} \pm \left(\mathbf{r} - \mathbf{p}_{n_e}^{\pm}\right) & \mathbf{r} \in T_{n_e}^{\pm} \\ \mathbf{0} & \mathbf{r} \notin T_{n_e}^{\pm} \end{cases}$$
(17c)

In the above equations, T_{n_f} is the n_f triangle and A_{n_f} is its area. Likewise, l_{n_e} is the length of edge n_e , $A_{n_e}^{\pm}$ is the area associated with triangles $T_{n_e}^{\pm}$, and $\mathbf{p}_{n_e}^{\pm}$ is the vertex of the triangle $T_{n_e}^{\pm}$ opposite the edge n_e [33].

With these basis functions, we can define $\underline{\mathcal{B}}^s$ and $\underline{\mathcal{B}}^v$ as

$$\underline{\mathcal{B}}^s = \begin{pmatrix} p_0 & \dots & p_{n_f} & \dots & p_{N_f} \end{pmatrix} \tag{18a}$$

$$\underline{\mathcal{B}}^{v} = \begin{pmatrix} \mathbf{f}_{0} & \dots & \mathbf{f}_{n_{e}} & \dots & \mathbf{f}_{N_{e}} \end{pmatrix}$$
 (18b)

with $N_s = N_f$ and $N_v = N_e$.

B. Discretized System

The discretized system for both the SPIE and VPIE are constructed through a Galerkin framework using inner products defined as

$$\langle g(\mathbf{r}), f(\mathbf{r}) \rangle = \int g^*(\mathbf{r}) f(\mathbf{r}) dS$$
 (19a)

$$\langle \mathbf{g}(\mathbf{r}), \mathbf{f}(\mathbf{r}) \rangle = \int \mathbf{g}^*(\mathbf{r}) \cdot \mathbf{f}(\mathbf{r}) dS$$
 (19b)

with * indicating complex conjugate and $g(\mathbf{r})$, $f(\mathbf{r})$, $g(\mathbf{r})$, and $f(\mathbf{r})$ denoting arbitrary functions (scalar and vector). For each region, we test (12) over the limiting surface as $\mathbf{r} \to \partial \Omega$ from within Ω_p and add the two systems together resulting in one system, coupled through the boundary conditions, that can be written as

$$\mathbb{Z}^{\chi} y^{\chi} = b^{\chi} \tag{20}$$

where the elements of this system are defined as

$$b_k^{\chi} = \sum_{p=1}^{2} \left\langle \underline{\mathcal{F}}_k^{\chi}, \underline{\mathcal{P}}_p^{\chi} \underline{\mathcal{W}}_p^{\chi} \boldsymbol{\tau}_p^{i^{\chi}} \right\rangle$$
 (21a)

$$\mathbb{Z}_{kn}^{\chi} = \sum_{p=1}^{2} \left\langle \underline{\mathcal{F}}_{k}^{\chi}, \underline{\mathcal{P}}_{p}^{\chi} \underline{\mathcal{W}}_{p}^{\chi} \left(\mathcal{I} - \mathcal{Z}_{p}^{\chi} \right) \circ \left(\left(\underline{\mathcal{P}}_{p}^{\chi} \right)^{-1} \underline{\mathcal{F}}_{n}^{\chi} \right) \right\rangle. \tag{21b}$$

Note, the sum is over the two regions (interior and exterior).

As the boundary conditions and scale factors manifest themselves as diagonal matrices, it is trivial to show that

$$b_k^{\chi} = \sum_{p=1}^{2} \bar{\mathcal{P}}_p^{\chi} \underline{\mathcal{W}}_p^{\chi} \left\langle \underline{\mathcal{F}}_k^{\chi}, \boldsymbol{\tau}_p^{i^{\chi}} \right\rangle$$
 (22a)

$$\mathbb{Z}_{kn}^{\chi} = \sum_{p=1}^{2} \underline{\bar{\mathcal{P}}}_{p}^{\chi} \underline{\bar{\mathcal{W}}}_{p}^{\chi} \left\langle \underline{\mathcal{F}}_{k}^{\chi}, \left(\mathcal{I} - \mathcal{Z}_{p}^{\chi} \right) \circ \underline{\mathcal{F}}_{n}^{\chi} \right\rangle \left(\underline{\bar{\mathcal{P}}}_{p}^{\chi} \right)^{-1} \tag{22b}$$

where $\underline{\bar{W}}_p^{\chi}$ and $\underline{\bar{P}}_p^{\chi}$ are also diagonal matrices with repeated elements of their unbarred counterparts.

Evaluating these operators with analytic basis sets can be performed exactly by exploiting the orthogonality of the spherical harmonics. An example of this for one operator is presented in Appendix E-A. The key challenge of working with piecewise tessellations is evaluating these operators when the k^{th} testing domain is close to the n^{th} basis domain. While a number of operators are familiar, some are not. To evaluate these integrals, we have taken a straightforward approach—singularity subtraction. There are certainly other methods of evaluating these integrals [34], but they are not necessary to demonstrate the crux of this paper—to prove the properties of the DPIE for discrete piecewise tessellations. To that end, we note that even though there are several unfamiliar operators, the singular integrals necessary are exactly the same as those used in the Electric Field Integral Equation (EFIE) and

Magnetic Field Integral Equation (MFIE); all other singular integrals can be evaluated via a combination of four base singular integrals. These singular integrals, along with an example of the complete treatment of one of the operators, is presented in Appendix E-B.

C. Zero-Mean Constraint

Finally, a critical component of a potential formulation is the zero-mean constraint. For analytical basis sets, this is accomplished by setting the coefficients of y_n^S and y_n^V associated with l=m=0 to zero. For coefficients of basis functions on tessellations, we use a Lagrange multiplier as in [35].

VI. RESULTS

In what follows, we present a collection of results that delineate the properties of the DPIE. Analytic basis set results are presented to demonstrate the characteristics of the SPIE and VPIE formulations themselves. The results presented in [32] are similar to what is presented here, however, the SPIE system was omitted and the VPIE system is different due to the changed boundary condition. After demonstrating the characteristics of the formulations discretized with spherical harmonics, results from the piecewise discretization are presented. The piecewise results will fall into two categories: (a) we will examine the correctness of the solution by comparing the RCS of objects against similar data obtained either from analytic calculations (Mie series using fields) or through numerical implementation of the PMCHWT [1] and Müller [2] formulations. (b) Next, we will present the condition number and number of iterations required to converge to an tolerance of 10^{-12} for a number of geometries. These sets of results are meant to ensure that not only are the resulting equations wellconditioned, but also converge rapidly as well. The dielectric objects will be immersed in freespace $\mu_{r1} = \epsilon_{r1} = 1$. Finally, we note the central theme of this paper is to demonstrate implementation of these formulations using well known basis sets and has not yet been paired with the fast multipole method. As a result, objects analyzed are not analytically large.

A. Analytic Basis Sets

The analytic analysis on a sphere gives insight to the behavior of the SPIE and VPIE. We begin with an analysis of scattering from a dielectric sphere with radius of $1\,\mathrm{m}$.

Note, the data presented in this section only deals with behavior of the system of equations. RCS data used for comparison in Section VI-B uses the Mie series solution, and as is to be expected, agrees with the RCS from the analytic method presented here.

We examine three scenarios with different material parameters. The orthogonality properties of spherical harmonics are used to isolate each harmonic's contribution in \mathbb{Z}^χ . After permuting rows and columns, we can arrive at a block-diagonal matrix $\mathbb{Z}^\chi = \operatorname{diag}\left(\mathbb{Z}^\chi|_0^0\dots\mathbb{Z}^\chi|_l^m\dots\mathbb{Z}^\chi|_{N_h}^{N_h}\right)$ for both the SPIE and VPIE. The frequencies examined in each scenario are limited to when $N_h = 2\lceil \max_p \Re\left(\kappa_p a\right) \rceil < 120$ where

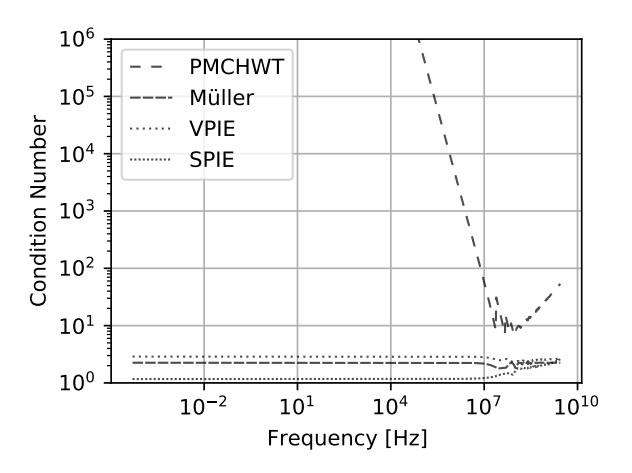


Fig. 1. Condition number for different band-limited integral equations across frequencies using analytic basis sets for a dielectric sphere with $\epsilon_{r2}=1.5$ and $\mu_{r2}=1/1.5$.

 $\Re\left(\kappa_p a\right)$ takes the real component of $\kappa_p a$. The finite dimensional expansion on the unknowns (equivalently, the operator), in effect creates a bandlimited version of the operator acting on the current. If the operator is compact, then this series converges and the condition number is representative of the system for which $N_h \to \infty$. As is well known, the PMCHWT integral equation, much like the EFIE, has a hyper-singular operator so the operator's true condition number is unbounded. This is what is represented in the figures.

Developing an analytical framework permits analysis on operators (both mapping as well as limiting properties). Some of this analysis was done in [32]. Here, we build to this body of work. Using the properties of the operators involved, it is possible to prove mapping properties of the vector operators. For both the VPIE presented here and [32], quantities represented using Ψ_l^m are mapped back to the same basis via the VPIE operators (ditto for Φ_l^m). This is as in [36, 37].

We will examine eigenvalues and condition numbers from the finite dimensional expansion of the operator. The eigenvalues are from the generalized eigenvalue problem, $Av = \lambda Bv$ with $A_{kn} = \mathbb{Z}_{kn}^{\chi}$ and $B_{kn} = \langle \underline{\mathcal{F}}_{k}^{\chi}, \underline{\mathcal{F}}_{n}^{\chi} \rangle$ (or equivalently the regular eigenvalue problem $B^{-1}Av = \lambda v$). Condition numbers are computed from the matrix $B^{-1}A$.

We apply the Lorenz gauge to arrive at the interface condition on the divergence of the magnetic vector potential. This results in slightly different behavior than was reported in [32]. Here, we examine effects of this change in boundary condition on the condition number of the band-limited VPIE for frequency ranges from $10\,\mu\text{Hz}$ to about $1\,\text{GHz}$, depending on material parameters. These are shown in Figures 1-3. The analysis covers the following three different cases for parameters: $n_1^2 = n_2^2$ in Figure 1, $n_1^2 \approx n_2^2$ in Figure 2, and $n_1^2 \not\approx n_2^2$ in Figure 3. From these figures some observations are in order: (a) the condition numbers are constant across frequencies wherein $\kappa_p \lesssim 2\pi$, (b) the condition number of the VPIE system is more sensitive to constitutive parameters, and (c) the behavior of the VPIE system is akin to that of the Müller systems. The boundary condition on the divergence of

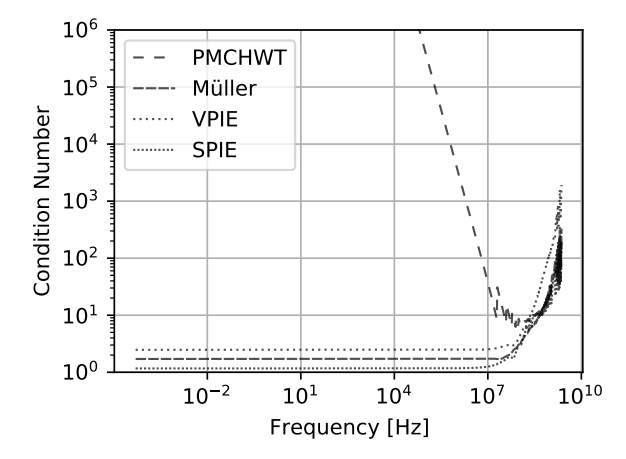


Fig. 2. Condition number for different band-limited integral equations across frequencies using analytic basis sets for a dielectric sphere with $\epsilon_{r2}=1.5$ and $\mu_{r2}=1$.

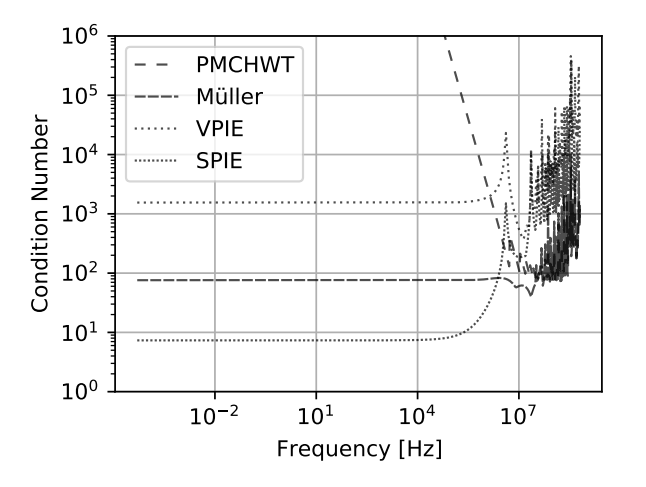


Fig. 3. Condition number for different band-limited integral equations across frequencies using analytic basis sets for a dielectric sphere with $\epsilon_{r2}=20$ and $\mu_{r2}=1$.

the magnetic vector potential does affect how well the hypersingular terms are cancelled. As a result the condition number is higher when the contrast is higher.

Next, we examine the eigenvalues of the SPIE and VPIE. To find these eigenvalues, we fist discretized the systems with spherical harmonics as before. We focus on the harmonics $n \in [1,10]$ and m=0, as representatives of the whole system, and let the frequency vary from $1\,\mathrm{MHz}$ to $1\,\mathrm{THz}$. For each of the harmonics and frequencies, we have a 2×2 and 6×6 matrix for the SPIE and VPIE respectively. Two and six eigenvalues per harmonic and frequency pair are computed and shown in Figures 4 and 5. From these figures, we can see that the eigenvalues accumulate away from 0 as the frequency goes to $0\,\mathrm{Hz}$ and are bounded.

B. Piecewise

The piecewise discretization is the crowning result of this paper. It serves to verify that the properties shown for canonical geometries commute to the complex shapes and

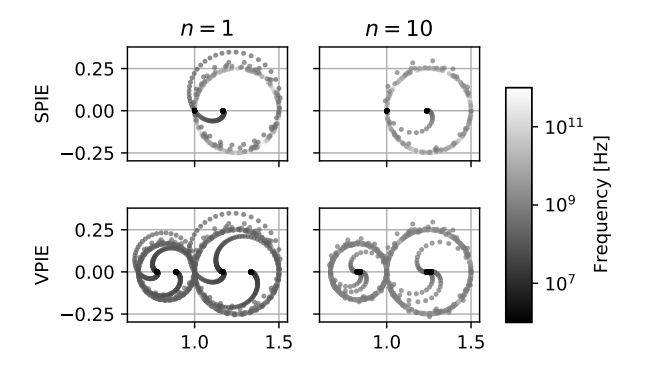


Fig. 4. Eigenvalues for the SPIE and VPIE for $\epsilon_{r2}=1.5$ and $\mu_{r2}=1/1.5$. The real and imaginary parts are plotted on the x- and y-axes respectively.

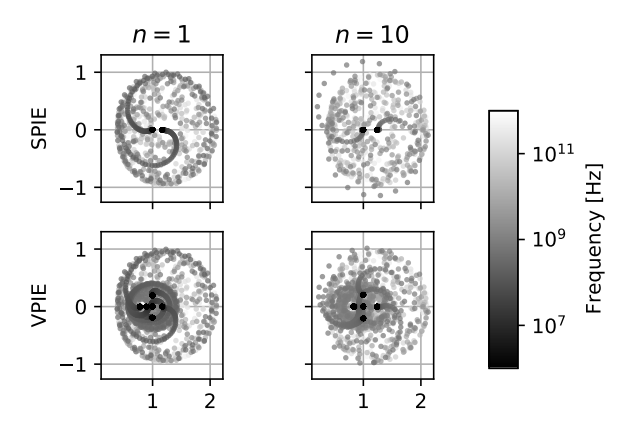


Fig. 5. Eigenvalues for the SPIE and VPIE for $\epsilon_{r2} = 1.5$ and $\mu_{r2} = 1$. The real and imaginary parts are plotted on the x- and y-axes respectively.

objects of actual interest. The incident waves here decompose $\mathbf{E}_1^i = \mathbf{E}_0 \exp{(-j\boldsymbol{\kappa}_1 \cdot \mathbf{r})}$ and are in the form found in [28]:

$$\phi_1^i = -\left(\mathbf{r} \cdot \mathbf{E}_0\right) \exp\left(-j\boldsymbol{\kappa}_1 \cdot \mathbf{r}\right) \tag{23a}$$

$$\mathbf{A}_{1}^{i} = -\frac{\boldsymbol{\kappa}_{1}}{\omega} \left(\mathbf{r} \cdot \mathbf{E}_{0} \right) \exp \left(-j \boldsymbol{\kappa}_{1} \cdot \mathbf{r} \right). \tag{23b}$$

All examples have the same constitutive parameters $\mu_2 = \mu_0$ and $\epsilon_2 = 1.5\epsilon_0$, and unless otherwise noted, use the same discretization across frequency.

1) Dielectric Sphere: We begin the piecewise analysis by considering the scattering from the same dielectric sphere with radius of 1 m. The sphere is meshed into 1280 patches and 1920 edges with an average edge length at 100 MHz of about $\lambda_1/19.9$. As predicted in Section VI-A, the condition number, show in Figure 6, is stable across frequencies. In this figure, the data is obtained for a set of frequencies starting at 100 MHz and decreasing it by a decade until 10 µHz. At 10 µHz, we reach the limits of double precision accuracy. Beyond this point, one would need to use extended precision, but the main arguments are sufficiently supported with this data. Specifically, the condition number across frequencies of the SPIE is about 53 and the VPIE is about 83 whereas those for PMCHWT are several orders of magnitude larger. It should be noted that the condition number of the Müller system is as good as that of the DPIEs.

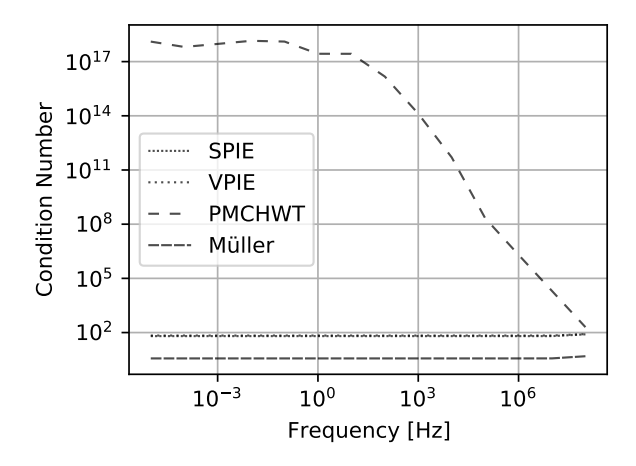


Fig. 6. Condition number for different integral equations across frequencies using piecewise basis sets for a dielectric sphere with $\epsilon_{r2}=1.5$ and $\mu_{r2}=1$.

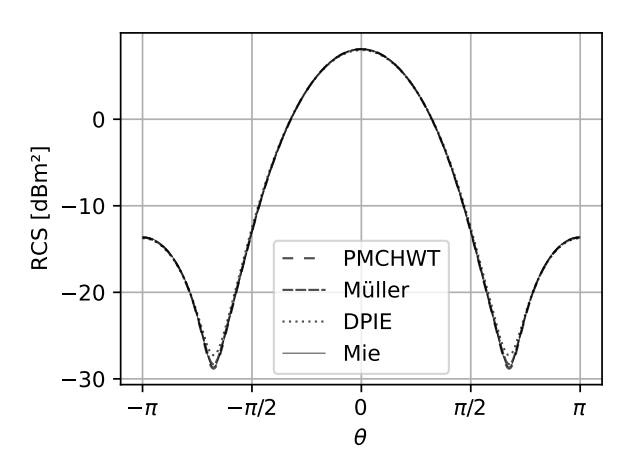


Fig. 7. RCS of the dielectric sphere at 100 MHz.

Next in Figures 7-9, we examine RCS data at three different frequencies, specifically at $100~\text{MHz},\,1~\text{Hz},\,\text{and}\,10~\text{\muHz}$ due to an incident wave directed along $\hat{\kappa}=-\hat{\mathbf{z}},\,$ polarized along $\mathbf{E}_0=\hat{\mathbf{x}},\,$ and measured at points along $\theta\in[-\pi,\pi]$ and $\phi=0.$ In Figure 7, we see that there is good agreement among all formulations including the analytic formulation at 100~MHz. In Figure 8, we see that the PMCHWT and Müller formulations have already diverged from the analytic solution at 1~Hz whereas the DPIE and Mie agree very well with each other. Finally, in Figure 9, we see that the DPIE still matches the analytic solution while the Müller solution is off the chart at around $-320~\text{dB}~\text{m}^2$ at $10~\text{\muHz}.$

Next, in addition to condition number, one typically cares about iteration count. For this experiment we used the same piecewise discretized sphere and, as before, data was collected from $10\,\mu\mathrm{Hz}$ to $100\,\mathrm{MHz}$. For this demonstration, we use the Quasi-Minimal Residual (QMR) but we have verified that other iterative solvers show similar behavior. A relative tolerance of 10^{-12} is used for two reasons. First, low frequency convergence, especially to $-350\,\mathrm{dB}\,\mathrm{m}^2$, necessitated the need for a smaller than typical tolerance and a relative as opposed

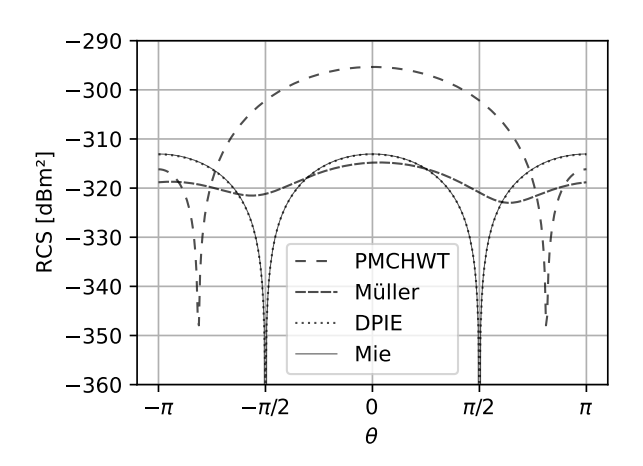


Fig. 8. RCS of the dielectric sphere at 1 Hz.

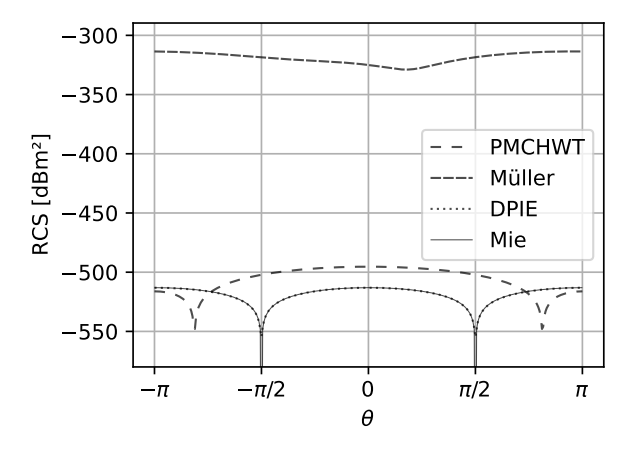


Fig. 9. RCS of the dielectric sphere at 10 µHz.

to absolute tolerance

$$||residual|| \le tol \times ||RHS||$$
. (24)

Second, as we examine convergence across frequencies, we wanted to keep the relative tolerance constant so that the iteration count comparison would be fair. The QMR solver is stopped after 500 iterations unless it stops due to a QMR related breakdown or the tolerance has been met. From Figure 10, it is apparent that the iteration count remains low as the frequency goes toward 0 Hz. It is also evident that PMCHWT requires significantly more iterations than the threshold except at 10 µHz where the iterative solver does converge within the tolerance but not to the correct solution. There is a moderate increase for the SPIE and VPIE as one tends to higher frequencies. This trend mirrors that seen in the Müller system [32]. We note that methods to mollify the behavior of Müller systems have been addressed by using intermediate Buffa-Christianssen basis sets [38], but investigating this phenomena lies outside the main goals of this paper and will be investigated in the future.

We turn our attention to the convergence of the iterative solver. In Figure 11, we see that the SPIE, VPIE, and Müller formulations converge very quickly in a few iterations to a solution within the relative tolerance specified. As mentioned

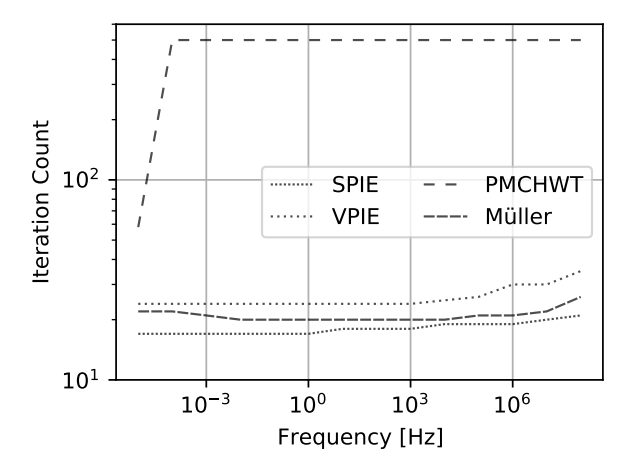


Fig. 10. Iteration count using QMR method for different integral equations across frequencies using RWG and pulse basis sets for a dielectric sphere with $\epsilon_{r2}=1.5$ and $\mu_{r2}=1$. The solver was stopped at 500 iterations if it had not converged yet.

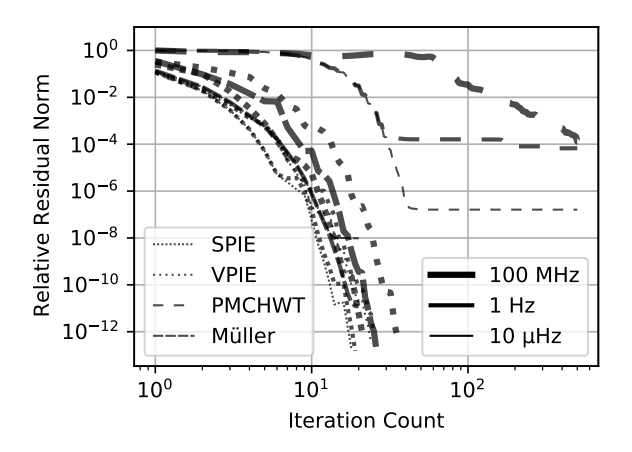


Fig. 11. Convergence plot of the relative residual $\|residual\|/\|RHS\|$ using the QMR method for different integral equations for a dielectric sphere with $\epsilon_{r2}=1.5$ and $\mu_{r2}=1$. The solver was stopped at 500 iterations if it had not converged yet. The color of the line indicates the formulation while the style (dotted, dashed, solid) indicates frequency.

above, the Müller formulation is well-conditioned but falls victim to the low-frequency breakdown due to how the electric and magnetic fields are represented. In other words, even though the solver finds a solution within a few iterations, it is worthless in the low-frequency regime.

Finally, we analyzed a dielectric sphere meshed with 20,480 patches and 30,720 edges. At $300\,\mathrm{MHz}$, the average edge length is about $\lambda_1/26.6$. The iteration counts for the SPIE and VPIE are 52 and 73 respectively. Müller converged in 42 iterations but PMCHWT only converged to 10^{-4} in 500 iterations. In Figure 12, we see that there is excellent agreement among all formulations at $300\,\mathrm{MHz}$.

2) Dielectric Almond: Next, we analyze scattering from a dielectric NASA almond, as seen in Figure 13. The NASA almond is meshed into 896 patches and 1344 edges. The average edge length at $100\,\mathrm{MHz}$ is about $\lambda_1/25.7$. First, the condition number data, shown in Figure 14, is stable across frequencies much like that observed for a sphere. The data

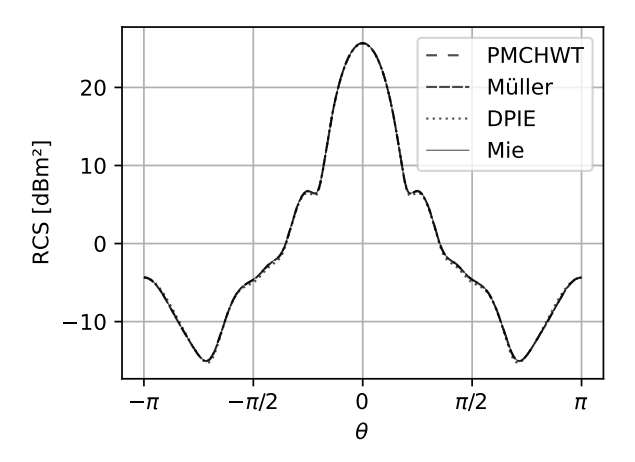


Fig. 12. RCS of the dielectric sphere at 300 MHz.

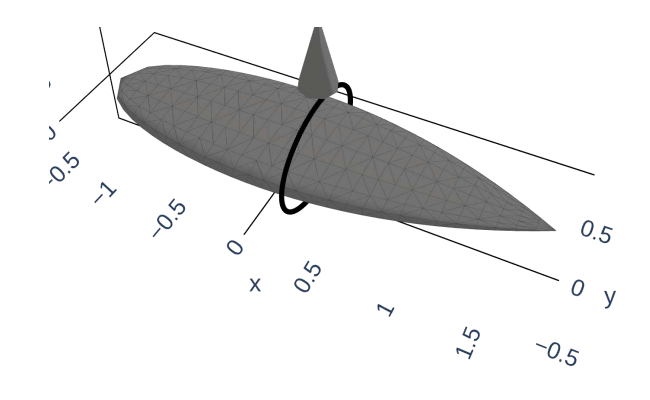


Fig. 13. NASA Almond geometry with incident and observation angles.

shown in the figure is for a range of frequencies from $100\,\mathrm{kHz}$ to $100\,\mathrm{MHz}$. As is evident the condition numbers for the SPIE and VPIE are relatively constant across the band whereas PMCHWT quickly blows up.

Next, the RCS is shown at $100\,\mathrm{MHz}$ with an incident wave directed along $\hat{\boldsymbol{\kappa}} = \hat{\mathbf{z}}$, polarization $\mathbf{E}_0 = \hat{\mathbf{y}}$, and measured

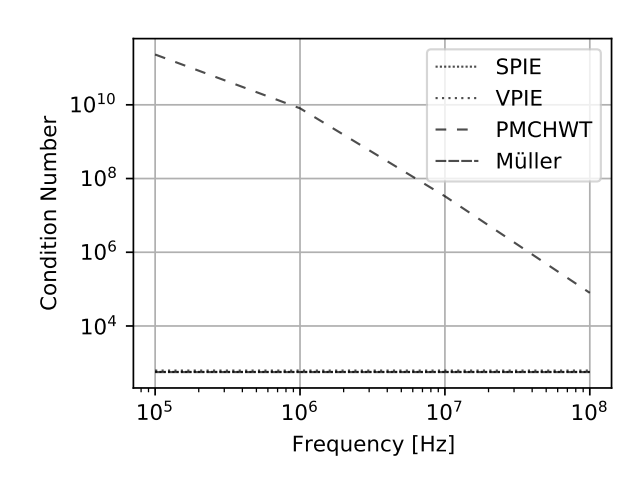


Fig. 14. Condition number for different integral equations across frequencies using piecewise basis sets for the dielectric NASA almond with $\epsilon_{r2}=1.5$ and $\mu_{r2}=1.$

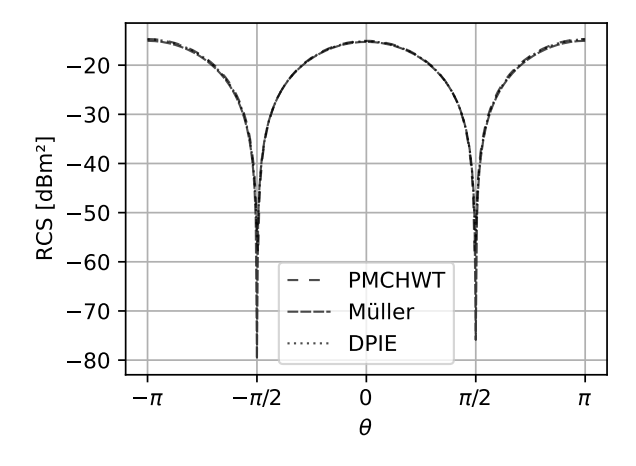


Fig. 15. RCS of the dielectric NASA almond at 100 MHz.

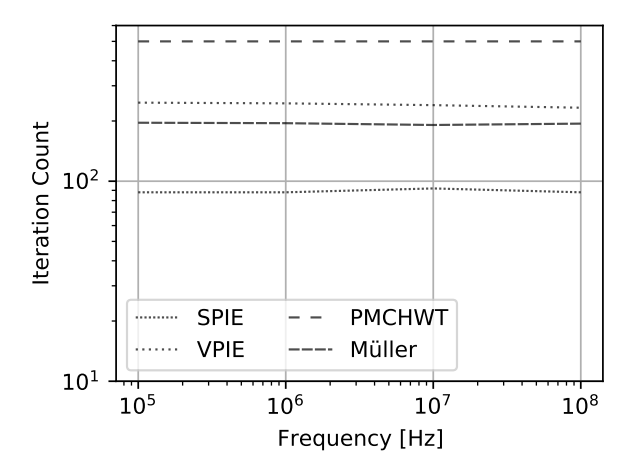


Fig. 16. Iteration count using QMR method for different integral equations across frequencies using piecewise basis sets for the dielectric NASA almond with $\epsilon_{r2}=1.5$ and $\mu_{r2}=1$. The solver was stopped at 500 iterations if it had not converged yet.

at points along $\theta \in [-\pi, \pi]$ and $\phi = \frac{\pi}{2}$. In Figure 15, we see that there is excellent agreement among all formulations at $100 \, \mathrm{MHz}$.

Next, the number of QMR iterations needed to converge to an error of 10^{-12} is shown in Figure 16 for the same frequency range. As before, the number of iterations is relatively constant for both the SPIE and VPIE. Overall, as is evident from Figures 14-16, the favorable properties of the SPIE and VPIE hold for non-canonical geometries.

3) Dielectric Arrowhead: Finally, we analyze scattering from a dielectric arrowhead, as seen in Figure 17. This is a challenging geometry in that it has sharp tips, and edges. The arrowhead is meshed into 23,024 patches and 34,536 edges. The average edge length at 100 MHz is about $^{\lambda_1}/_{19.9}$. Given the size of the problem, we just present the data for scattering from a 100 MHz incident wave directed along $\hat{\mathbf{k}} = \hat{\mathbf{z}}$, polarization $\mathbf{E}_0 = \hat{\mathbf{y}}$, and measured at points along $\theta \in [-\pi,\pi]$ and $\phi = \frac{\pi}{2}$. incident. The SPIE and VPIE converge to a relative error of 10^{-12} , with iteration counts of 75 and 90. Müller converged in 50 iterations but PMCHWT only converged to 10^{-3} in 500 iterations. The RCS of this

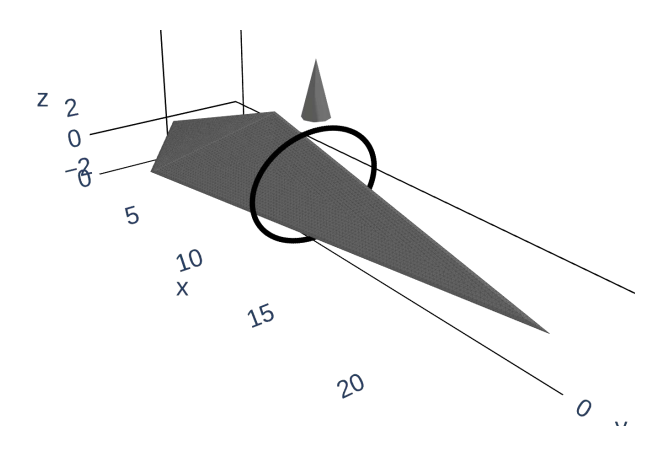


Fig. 17. Arrowhead geometry with incident and observation angles

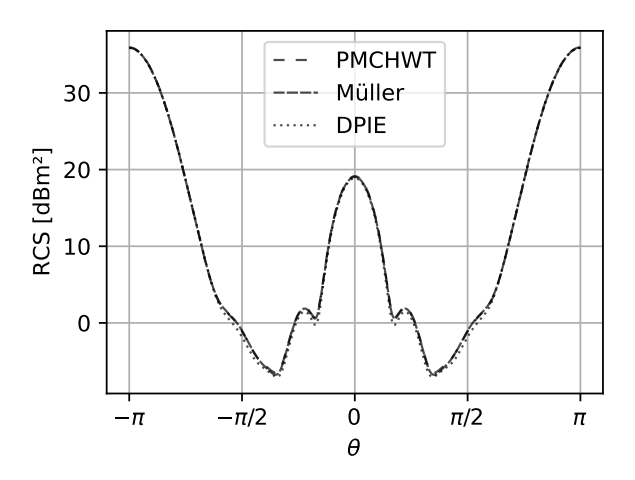


Fig. 18. RCS of the dielectric arrowhead at 100 MHz.

scatterer is shown in Figure 18. As before, we see that there is very good agreement among all formulations at this frequency.

VII. SUMMARY

This paper presents a rather detailed implementation of the DPIE on discrete piecewise tessellations. As is observed in canonical geometries, the discrete piecewise system is well-conditioned and converges rapidly. Analysis is presented using analytic basis sets for both the SPIE and VPIE, which explores condition number across frequencies. While it may seem to be computationally daunting due to the increased number of operators and number of unknowns, and this was indeed a bottleneck in some of the results presented here, this approach is amenable to acceleration using fast multipole based methods. This, further analysis into alternate VPIE scaling weights/formulations, and extension to composite objects will be presented in upcoming papers.

APPENDIX A DEFINITION OF DPIE OPERATORS

The integral operators defined in this paper are as follows:

$$S_{p} \circ \begin{pmatrix} \mathbf{x} \\ x \end{pmatrix}^{T} = \int G_{p}(\mathbf{r}, \mathbf{r}') \begin{pmatrix} \mathbf{x} (\mathbf{r}') \\ x (\mathbf{r}') \end{pmatrix}^{T} dS'$$
 (25a)

$$\mathcal{D}_p \circ x = -\nabla \cdot \mathcal{S}_p \circ (\hat{\mathbf{n}}_p x) \tag{25b}$$

$$\mathcal{N}_p \circ x = -\hat{\mathbf{n}}_p \cdot \nabla \nabla \cdot \mathcal{S}_p \circ (\hat{\mathbf{n}}_p x)$$
 (25c)

$$\mathcal{D}'_{n} \circ x = \hat{\mathbf{n}}_{n} \cdot \nabla \mathcal{S}_{p} \circ x \tag{25d}$$

$$\mathcal{K}'_{p} \circ \mathbf{x} = -\nabla \times \mathcal{S}_{p} \circ (\hat{\mathbf{n}}_{p} \times \mathbf{x})$$
 (25e)

$$\mathcal{J}_{n}^{2} \circ \mathbf{x} = \hat{\mathbf{n}}_{n} \times \mathcal{S}_{p} \circ (\hat{\mathbf{n}}_{n} \times \mathbf{x})$$
 (25f)

$$\mathcal{J}_p^3 \circ \mathbf{x} = \hat{\mathbf{n}}_p \cdot \mathcal{S}_p \circ \left(\hat{\mathbf{n}}_p \times \mathbf{x} \right) \tag{25g}$$

$$\mathcal{J}_p^4 \circ \mathbf{x} = \nabla \cdot \mathcal{S}_p \circ \left(\hat{\mathbf{n}}_p \times \mathbf{x} \right) \tag{25h}$$

$$\mathcal{L}_{p} \circ \mathbf{x} = \frac{1}{\kappa_{-}^{2}} \nabla \times \nabla \times \mathcal{S}_{p} \circ \mathbf{x}$$
 (25i)

$$\mathcal{K}_p \circ \mathbf{x} = \hat{\mathbf{n}}_p \times \nabla \times \mathcal{S}_p \circ \mathbf{x} \tag{25j}$$

$$\mathcal{M}_{p}^{3} \circ \mathbf{x} = \hat{\mathbf{n}}_{p} \cdot \nabla \times \mathcal{S}_{p} \circ \mathbf{x}$$
 (25k)

$$\mathcal{P}_{n}^{2} \circ x = \hat{\mathbf{n}}_{n} \times \nabla \mathcal{S}_{p} \circ x \tag{251}$$

$$Q_p^1 \circ x = \hat{\mathbf{n}}_p \times \hat{\mathbf{n}}_p \times \nabla \times S_p \circ (\hat{\mathbf{n}}_p x)$$
 (25m)

$$Q_n^2 \circ x = \hat{\mathbf{n}}_n \times \mathcal{S}_p \circ (\hat{\mathbf{n}}_n x) \tag{25n}$$

$$Q_p^3 \circ x = \hat{\mathbf{n}}_p \cdot \mathcal{S}_p \circ (\hat{\mathbf{n}}_p x). \tag{250}$$

We denote adjoint operators with a prime. Additionally, we introduce the shorthand for operators $\mathcal{O}_p^t = \hat{\mathbf{n}}_p \times \hat{\mathbf{n}}_p \times \mathcal{O}_p$.

APPENDIX B SPHERICAL HARMONICS

Next, we define the scalar and vector spherical harmonics used for the analytic basis sets.

$$Y_l^m(\mathbf{r}) = \sqrt{\frac{2l+1}{4\pi} \frac{(l-m)!}{(l+m)!}} P_l^m(\cos \theta) e^{jm\phi}$$
 (26a)

$$\mathbf{\Psi}_{l}^{m}(\hat{\mathbf{r}}) = -\hat{\mathbf{r}} \times \mathbf{\Phi}_{l}^{m}(\hat{\mathbf{r}}) = c_{l} r \nabla Y_{l}^{m}(\hat{\mathbf{r}})$$
(26b)

$$\mathbf{\Phi}_{l}^{m}\left(\hat{\mathbf{r}}\right) = \hat{\mathbf{r}} \times \mathbf{\Psi}_{l}^{m}\left(\hat{\mathbf{r}}\right) = c_{l}\mathbf{r} \times \nabla \mathbf{Y}_{l}^{m}\left(\hat{\mathbf{r}}\right)$$
(26c)

$$c_{l} = \begin{cases} 1 & l = 0\\ \frac{1}{\sqrt{l(l+1)}} & l \neq 0 \end{cases}$$
 (26d)

with $\mathrm{P}_l^m(\cos\theta)$ denoting associated Legendre polynomials, $l \geq 0$, and $|m| \leq l$. The scaling factor c_l is used to orthonormalize $\mathbf{\Psi}_l^m$ and $\mathbf{\Phi}_l^m$ which is not strictly necessary but eases the derivation. Spherical Bessel functions are denoted using

$$b_{l}^{(\alpha)}(z) = \begin{cases} j_{l}(z) & \alpha = 1\\ y_{l}(z) & \alpha = 2\\ h_{l}^{(1)}(z) & \alpha = 3\\ h_{l}^{(2)}(z) & \alpha = 4 \end{cases}$$
(27)

where the index α is used to denote the type and/or the kind. Using these definitions, the scalar and vector spherical wave functions are as follows:

$$\varphi_{lm}^{(\alpha)}(\kappa, \mathbf{r}) = c_l \, \mathbf{b}_l^{(\alpha)}(\kappa r) \, \mathbf{Y}_l^m(\hat{\mathbf{r}})$$
 (28a)

$$\mathbf{L}_{lm}^{(\alpha)}(\kappa, \mathbf{r}) = \nabla \varphi_{lm}^{(\alpha)}(\kappa, \mathbf{r}) \tag{28b}$$

$$\mathbf{M}_{lm}^{(\alpha)}(\kappa, \mathbf{r}) = \frac{1}{\kappa} \nabla \times \mathbf{N}_{lm}^{(\alpha)}(\kappa, \mathbf{r}) = -\mathbf{r} \times \nabla \varphi_{lm}^{(\alpha)}(\kappa, \mathbf{r})$$
(28c)

$$\mathbf{N}_{lm}^{(\alpha)}(\kappa, \mathbf{r}) = \frac{1}{\kappa} \nabla \times \mathbf{M}_{lm}^{(\alpha)}(\kappa, \mathbf{r})$$
 (28d)

Note, in addition to the usual $\mathbf{M}_{lm}^{(\alpha)}(\kappa, \mathbf{r})$ and $\mathbf{N}_{lm}^{(\alpha)}(\kappa, \mathbf{r})$ one need to use $\mathbf{L}_{lm}^{(\alpha)}(\kappa, \mathbf{r})$ to represent the magnetic vector potential [39].

APPENDIX C PLANEWAVE EXPANSION

For completeness, we include a scalar and vector planewave expansion in terms of spherical wave functions.

$$\exp\left(-j\kappa\hat{\mathbf{z}}\cdot\mathbf{r}\right) = \sum_{l=0}^{\infty} \sum_{m=-l}^{l} a_{lm}\,\varphi_{lm}^{(1)}\left(\kappa,\mathbf{r}\right)$$
(29a)

$$\hat{\mathbf{x}} \exp(-j\kappa \hat{\mathbf{z}} \cdot \mathbf{r}) = \sum_{l=0}^{\infty} \sum_{m=-l}^{l} b_{lm} \,\mathbf{M}_{lm}^{(1)}(\kappa, \mathbf{r}) + c_{lm} \,\mathbf{N}_{lm}^{(1)}(\kappa, \mathbf{r})$$
(29b)

with

$$a_{lm} = \begin{cases} \frac{j^{-l}}{c_l} \sqrt{4\pi (2l+1)} & m=0\\ 0 & m \neq 0 \end{cases}$$
 (30a)

$$b_{lm} = \begin{cases} \frac{j^{-l+|m|}}{c_l} \sqrt{\pi \frac{2l+1}{l(l+1)}} & |m| = 1\\ 0 & |m| \neq 1 \end{cases}$$
 (30b)

$$c_{lm} = \begin{cases} \frac{j^{-l+m}}{c_l} \sqrt{\pi \frac{2l+1}{l(l+1)}} & |m| = 1\\ 0 & |m| \neq 1 \end{cases}.$$
 (30c)

APPENDIX D GREEN'S FUNCTION EXPANSION

The final ingredients necessary for analytic evaluation of the integrals in the DPIE are the expansion of the Green's functions. The scalar and dyadic Green's function expansions are

$$G_p = j\kappa_p \sum_{l=0}^{\infty} \frac{1}{c_l^2} \sum_{m=-l}^{l} \varphi_{lm}^{(\alpha_p)} \left(\kappa_p, \mathbf{r}\right) \varphi_{lm}^{(\beta_p)*} \left(\kappa_p^*, \mathbf{r}'\right)$$
(31a)

$$\underline{\underline{G}}_{p} = j\kappa_{p} \sum_{l=0}^{\infty} \frac{1}{g_{l}c_{l}^{2}} \sum_{m=-l}^{l} \mathbf{M}_{lm}^{(\alpha_{p})} \left(\kappa_{p}, \mathbf{r}\right) \mathbf{M}_{lm}^{(\beta_{p})*} \left(\kappa_{p}^{*}, \mathbf{r}'\right) + \mathbf{N}_{lm}^{(\alpha_{p})} \left(\kappa_{p}, \mathbf{r}\right) \mathbf{N}_{lm}^{(\beta_{p})*} \left(\kappa_{p}^{*}, \mathbf{r}'\right)$$

with

$$\alpha_p = \begin{cases} 4 & p = 1\\ 1 & p = 2 \end{cases} \tag{32a}$$

$$\beta_p = \begin{cases} 1 & p = 1\\ 3 & p = 2 \end{cases} \tag{32b}$$

$$g_l = \begin{cases} 1 & l = 0 \\ l(l+1) & l \neq 0 \end{cases}$$
 (32c)

These expressions together with the spherical harmonics and wave functions constitute the underpinnings of our analytical analysis.

APPENDIX E CANDIDATE INNER PRODUCT EVALUATION

As there are a number of different inner products to be evaluated, it is cumbersome to provide a detailed prescription of each. Indeed, for the DPIE, there are 15 unique operators. As most of these follow the same template, we provide one illustrative example while leaving the reader with the necessary tools to flesh out the others.

Our example is one that is less commonly encountered: \mathbb{Z}^V for the operator \mathcal{P}_p^2 . For the purposes of illustration, we will focus on a single region and omit the scaling matrices as these are diagonal and do not add to the integral. Specifically,

$$\left. \tilde{\mathbb{Z}}_{23,p}^{V} \right|_{kn} = \left\langle \underline{\mathcal{B}}_{k}^{v}, \hat{\mathbf{n}}_{p} \times \nabla \mathcal{S}_{p} \circ \underline{\mathcal{B}}_{n}^{s} \right\rangle \tag{33}$$

where $k \in [0, N_v)$ and $n \in [0, N_s)$ are the testing and basis indices for this block of $\tilde{\mathbb{Z}}^V$.

A. Analytic evaluation

For analytic analysis, we use (16a) and (16b). If we let testing index k correspond to harmonic indices l and m for Ψ when $k < (N_h + 1)^2$ and for Φ when $k \ge (N_h + 1)^2$, and basis index n correspond to harmonic indices l' and m', it is easy to see that we can take advantage of the orthogonality of the spherical harmonics. When $l \ne l'$ or $m \ne m'$ (in other words $\mod\left(k,(N_h+1)^2\right)\ne n$), then the system element is zero. This allows us to focus on a specific harmonic specified by l and m. We analyze the two cases when k selects a testing function from $\underline{\mathcal{B}}_{\Psi}$ and $\underline{\mathcal{B}}_{\Phi}$:

$$\tilde{\mathbb{Z}}_{23,p}^{V,\mathbf{\Psi}}\Big|_{lm} = \left\langle \mathbf{\Psi}_{l}^{m}\left(\mathbf{r}\right), \hat{\mathbf{n}}_{p} \times \nabla \mathcal{S}_{p} \circ \mathbf{Y}_{l}^{m} \right\rangle = 0$$

$$\tilde{\mathbb{Z}}_{23,p}^{V,\mathbf{\Phi}}\Big|_{lm} = \left\langle \mathbf{\Phi}_{l}^{m}\left(\mathbf{r}\right), \hat{\mathbf{n}}_{p} \times \nabla \mathcal{S}_{p} \circ \mathbf{Y}_{l}^{m} \right\rangle$$

$$= -\varepsilon_{p} \frac{j\kappa_{p}}{c_{l}^{2}} \left\langle \mathbf{\Psi}_{l}^{m}\left(\mathbf{r}\right), \mathbf{L}_{lm}^{(\alpha_{p})}\left(\kappa_{p}, \mathbf{r}\right) \right\rangle$$

$$\left\langle \mathbf{Y}_{l}^{m}\left(\hat{\mathbf{r}}'\right), \varphi_{lm}^{(\beta_{p})}\left(\kappa_{p}, \mathbf{r}'\right) \right\rangle^{*}.$$
(34)

B. Evaluation on Discrete Patches

Next, we briefly prescribe evaluation of all inner products that are necessary. As alluded to earlier, we use singularity subtraction and decide to subtract the first two terms from the Taylor series expansion of the exponential function. As will

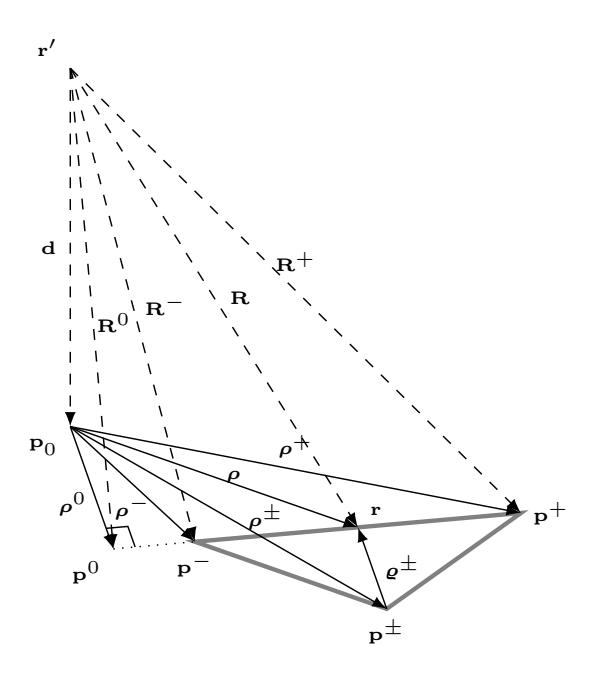


Fig. 19. Vector and point definitions for singular integration.

be evident, the singular integrals needed are identical to the ones needed for the EFIE and MFIE and can be found in [40, 41]. It follows that, if necessary, one can use better rules [34, 42, 43], but this is not the crux of the presented work. We use Figure 19 to set the stage for definitions, and it is here purely for completeness. The definitions here follow those in [40].

It is well known that the following integrals can be evaluated analytically as we approach the patch.

$$\mathcal{I}_{\frac{1}{R}} = \int \frac{1}{R} dS \tag{35a}$$

$$\mathcal{I}_{\frac{\rho}{R}} = \int \frac{\rho}{R} dS \tag{35b}$$

$$\mathcal{I}_{\frac{1}{R^3}} = \int \frac{1}{R^3} dS \tag{35c}$$

$$\mathcal{I}_{\frac{\rho}{R^3}} = \int \frac{\rho}{R^3} dS \tag{35d}$$

To effect the integration, we used a seven point Gauss-Legendre rules for the integrals over a patch. For the hypersingular integral in the SPIE, there is a line integral and a fourteen point Gauss-Legendre rule was employed.

As an aside, two issues naturally crop up when surfaces are modeled using higher order geometric representations—(a) evaluation of singular integrals and (b) cost of a higher quadrature rule. The integrals in (35) have been dealt with in the community using either a mapping of the contour to a flat patch which allows the use of singularity subtraction or singularity cancellation techniques. Amelioration of the costs associated with evaluation of these integrals higher order geometries have been dealt with in [44, 45] by integrating with a wideband fast multipole method which uses a combination of an adaptive quadrature rule and singularity cancellation around a small neighborhood of the singularity.

The techniques used in this paper rely on the fact that we are using a flat tessellation. To illustrate a general approach,

consider the evaluation of $\tilde{\mathbb{Z}}_{23,p}^V$. The integration is typically over T_k^\pm and T_n . To simplify the presentation, only consider T_k^+ (the other follow trivially). Given that $\hat{\mathbf{n}}_p$ is constant over T_k^+ , manipulation of the integral results in

$$\tilde{\mathbb{Z}}_{23,p}^{V}\Big|_{kn} = \int_{T_{n}} p_{n}\left(\mathbf{r}'\right) \hat{\mathbf{n}}_{p} \cdot \int_{T^{+}} \nabla G_{p} \times \mathbf{f}_{k}\left(\mathbf{r}\right) dS dS'. \quad (36)$$

As is usually done using singularity subtraction, we get both an integral with a removable singularity and a non-singular integral that can be evaluated numerically. We only discuss the singular portion of the integral that is denoted below using |S|. For (36), this can be written as

$$\tilde{\mathbb{Z}}_{23,p}^{V}\Big|_{kn}^{S} = -\frac{1}{4\pi} \int_{T_{n}} p_{n} \left(\mathbf{r}'\right) \hat{\mathbf{n}}_{p} \cdot \left(\int_{T_{k}^{+}} \frac{\mathbf{R}}{R^{3}} \times \mathbf{f}_{k} \left(\mathbf{r}\right) dS + \frac{\kappa_{p}^{2}}{2} \int_{T_{k}^{+}} \frac{\mathbf{R}}{R} \times \mathbf{f}_{k} \left(\mathbf{r}\right) dS \right) dS'$$
(37)

It follows, that to evaluate this integral we need to evaluate $\int \frac{\mathbf{R}}{R^3} \times \mathbf{f}_k(\mathbf{r}) \, dS$ and $\int \frac{\mathbf{R}}{R} \times \mathbf{f}_k(\mathbf{r}) \, dS$. From (35), one can derive the following analytic integrals:

$$\mathcal{I}_{\frac{\mathbf{R}}{R}} = \int \frac{\mathbf{R}}{R} dS = \mathcal{I}_{\frac{\boldsymbol{\rho}}{R}} + \mathbf{d}\mathcal{I}_{\frac{1}{R}}$$

$$\mathcal{I}_{\frac{\mathbf{R}}{R} \times \mathbf{f}_{n}} = \int_{n}^{\pm} \frac{\mathbf{R}}{R} \times \mathbf{f}_{n}(\mathbf{r}) dS = \pm \frac{l_{n}}{2A_{n}^{\pm}} \left(\mathbf{d} + \boldsymbol{\rho}^{\pm} \right) \times \mathcal{I}_{\frac{\mathbf{R}}{R}}$$
(38a)
$$(38a)$$

$$\mathcal{I}_{\frac{\mathbf{f}_n}{R}} = \int_n^{\pm} \frac{\mathbf{f}_n(\mathbf{r})}{R} dS = \pm \frac{l_n}{2A_n^{\pm}} \left(\mathcal{I}_{\frac{\boldsymbol{\rho}}{R}} - \boldsymbol{\rho}^{\pm} \mathcal{I}_{\frac{1}{R}} \right)$$
 (38c)

$$\mathcal{I}_{\frac{\mathbf{R}}{R^3}} = \int \frac{\mathbf{R}}{R^3} dS = \mathcal{I}_{\frac{\rho}{R^3}} + \mathbf{d}\mathcal{I}_{\frac{1}{R^3}}$$
 (38d)

$$\mathcal{I}_{\frac{\mathbf{R}}{R^{3}}\times\mathbf{f}_{n}}=\int_{n}^{\pm}\frac{\mathbf{R}}{R^{3}}\times\mathbf{f}_{n}\left(\mathbf{r}\right)dS=\pm\frac{l_{n}}{2A_{n}^{\pm}}\left(\mathbf{d}+\boldsymbol{\rho}^{\pm}\right)\times\mathcal{I}_{\frac{\mathbf{R}}{R^{3}}}.\tag{38e}$$

The integral $\mathcal{I}_{\frac{\mathbf{f}_n}{R}}$ is not necessary for this example but is necessary for the other operators. The process for addressing the rest of the singular integrals follow a similar process. Note, the singular integrals are either due to G_p or ∇G_p , are over either testing or source domains, and can all be formed as combinations of (35). Just as the normal over each triangle is constant due to the flat-tessellation, $\hat{\mathbf{n}} \cdot \mathbf{R}$ and $\hat{\mathbf{n}}' \cdot \mathbf{R}$ are also constant over the testing and source domains respectively. Below the expressions that we use to treat the singular integrals are cataloged. They are one of several equivalent expressions that can be used for singularity subtraction.

For the SPIE, the singular integrals needed for each operator are as follows:

$$\tilde{\mathbb{Z}}_{11,p}^{S}\Big|_{kn}^{S} = \int_{T_{k}} \left(\hat{\mathbf{n}}_{p}' \cdot \mathbf{R} \right) \left(\mathcal{I}_{\frac{1}{R^{3}}} + \frac{\kappa_{p}^{2}}{2} \mathcal{I}_{\frac{1}{R}} \right) dS \qquad (39a)$$

$$\tilde{\mathbb{Z}}_{12,p}^{S}\Big|_{kn}^{S} = -\int_{T_{\cdot}} \mathcal{I}_{\frac{1}{R}} - j\kappa_{p} A_{n} dS \tag{39b}$$

$$\tilde{\mathbb{Z}}_{22,p}^{S}\Big|_{kn}^{S} = \int_{T_n} \left(\hat{\mathbf{n}}_p \cdot \mathbf{R}\right) \left(\mathcal{I}_{\frac{1}{R^3}} + \frac{\kappa_p^2}{2} \mathcal{I}_{\frac{1}{R}}\right) dS'.$$
 (39c)

The $\tilde{\mathbb{Z}}_{22,p}^S$ operator is hyper-singular and is dealt with as in [46] rather than with singularity subtraction.

For the VPIE, the singular integrals needed for each operator are as follows:

$$\tilde{\mathbb{Z}}_{11,p}^{V}\Big|_{kn}^{S} = \int_{T_{n}^{+}} \left(\hat{\mathbf{n}}_{p}' \times \mathbf{f}_{n}'\right) \cdot \left(\mathcal{I}_{\frac{\mathbf{R}}{R^{3}} \times \mathbf{f}_{k}} + \frac{\kappa_{p}^{2}}{2} \mathcal{I}_{\frac{\mathbf{R}}{R} \times \mathbf{f}_{k}}\right) dS' \tag{40a}$$

$$\left. \tilde{\mathbb{Z}}_{12,p}^{V} \right|_{kn}^{S} = \int_{T_{t}^{+}} \nabla_{s} \cdot \mathbf{f}_{k} \nabla_{s}' \cdot \mathbf{f}_{n}' \left(\mathcal{I}_{\frac{1}{R}} - j \kappa_{p} A_{n}^{+} \right)$$

$$-\kappa_p^2 \mathbf{f}_k \cdot \left(\mathcal{I}_{\frac{\mathbf{f}'_n}{R}} - j\kappa_p \int_{\mathcal{T}^+} \mathbf{f}'_n dS' \right) dS \qquad (40b)$$

$$\left. \tilde{Z}_{13,p}^{V} \right|_{k_{B}}^{S} = 0$$
 (40c)

$$\tilde{\mathbb{Z}}_{14,p}^{V}\Big|_{kn}^{S} = \int_{T_{-}^{\pm}} \hat{\mathbf{n}}_{p}' \cdot \left(\mathcal{I}_{\frac{\mathbf{R}}{R^{3}} \times \mathbf{f}_{k}} + \frac{\kappa_{p}^{2}}{2} \mathcal{I}_{\frac{\mathbf{R}}{R} \times \mathbf{f}_{k}} \right) dS' \qquad (40d)$$

$$\left. \tilde{\mathbb{Z}}_{21,p}^{V} \right|_{kn}^{S} = \int_{T_{h}^{+}} \left(\hat{\mathbf{n}}_{p} \times \mathbf{f}_{k} \right)$$

$$\cdot \left(\hat{\mathbf{n}}'_p \times \left(\mathcal{I}_{\frac{\mathbf{r}'_n}{R}} - j\kappa_p \int_{T^+} \mathbf{f}'_n dS' \right) \right) dS \quad (40e)$$

$$\tilde{\mathbb{Z}}_{22,p}^{V}\Big|_{kn}^{S} = \int_{T_{k}^{+}} \left(\hat{\mathbf{n}}_{p} \times \mathbf{f}_{k}'\right) \cdot \left(\mathcal{I}_{\frac{\mathbf{R}}{R^{3}} \times \mathbf{f}_{n}'} + \frac{\kappa_{p}^{2}}{2} \mathcal{I}_{\frac{\mathbf{R}}{R} \times \mathbf{f}_{n}'}\right) dS \tag{40f}$$

$$\tilde{\mathbb{Z}}_{23,p}^{V}\Big|_{kn}^{S} = \int_{T_{n}^{+}} \hat{\mathbf{n}}_{p} \cdot \left(\mathcal{I}_{\frac{\mathbf{R}}{R^{3}} \times \mathbf{f}_{k}} + \frac{\kappa_{p}^{2}}{2} \mathcal{I}_{\frac{\mathbf{R}}{R} \times \mathbf{f}_{k}} \right) dS' \qquad (40g)$$

$$\tilde{\mathbb{Z}}_{24,p}^{V}\Big|_{kn}^{S} = \int_{T_{n}^{+}} \hat{\mathbf{n}}_{p}' \cdot \hat{\mathbf{n}}_{p} \times \left(\mathcal{I}_{\frac{\mathbf{f}_{k}}{R}} - j\kappa_{p} \int_{T_{k}^{+}} \mathbf{f}_{k} dS\right) dS' \tag{40h}$$

$$\tilde{\mathbb{Z}}_{31,p}^{V}\Big|_{kn}^{S} = \int_{T_{n}^{+}} \hat{\mathbf{n}}_{p} \cdot \hat{\mathbf{n}}'_{p} \times \left(\mathcal{I}_{\frac{\mathbf{f}'_{n}}{R}} - j\kappa_{p} \int_{T_{n}^{+}} \mathbf{f}'_{n} dS'\right) dS \tag{40i}$$

$$\left. \tilde{\mathbb{Z}}_{32,p}^{V} \right|_{kn}^{S} = -\int_{T_{k}^{+}} \hat{\mathbf{n}}_{p} \cdot \left(\mathcal{I}_{\frac{\mathbf{R}}{R^{3}} \times \mathbf{f}'_{n}} + \frac{\kappa_{p}^{2}}{2} \mathcal{I}_{\frac{\mathbf{R}}{R} \times \mathbf{f}'_{n}} \right) dS \quad (40j)$$

$$\left. \tilde{\mathbb{Z}}_{33,p}^{V} \right|_{kn}^{S} = \int_{T_n^+} \left(\hat{\mathbf{n}}_p \cdot \mathbf{R} \right) \left(\mathcal{I}_{\frac{1}{R^3}} + \frac{\kappa_p^2}{2} \mathcal{I}_{\frac{1}{R}} \right) dS'$$
 (40k)

$$\tilde{\mathbb{Z}}_{34,p}^{V}\Big|_{kn}^{S} = -\int_{T_{+}^{+}} \hat{\mathbf{n}}_{p} \cdot \hat{\mathbf{n}}' \left(\mathcal{I}_{\frac{1}{R}} - j\kappa_{p} A_{n}^{+} \right) dS$$
 (401)

$$\tilde{\mathbb{Z}}_{41,p}^{V}\Big|_{kn}^{S} = -\int_{T_{k}^{+}} \hat{\mathbf{n}}_{p}' \cdot \left(\mathcal{I}_{\frac{\mathbf{R}}{R^{3}} \times \mathbf{f}_{n}'} + \frac{\kappa_{p}^{2}}{2} \mathcal{I}_{\frac{\mathbf{R}}{R} \times \mathbf{f}_{n}'}\right) dS \quad (40\text{m})$$

$$\tilde{\mathbb{Z}}_{42,p}^{V}\Big|_{bn}^{S} = 0$$
 (40n)

$$\tilde{\mathbb{Z}}_{43,p}^{V}\Big|_{kn}^{S} = \int_{T_{\cdot}^{+}} \kappa_{p}^{2} \left(\mathcal{I}_{\frac{1}{R}} - j\kappa_{p} A_{n}^{+} \right) dS \tag{400}$$

$$\left. \tilde{\mathbb{Z}}_{44,p}^{V} \right|_{kn}^{S} = \int_{T_{t}^{+}} \left(\hat{\mathbf{n}}_{p}^{\prime} \cdot \mathbf{R} \right) \left(\mathcal{I}_{\frac{1}{R^{3}}} + \frac{\kappa_{p}^{2}}{2} \mathcal{I}_{\frac{1}{R}} \right) dS \qquad (40p)$$

The integrals $\int_{T_k^+} \mathbf{f}_k dS$ and $\int_{T_n^+} \mathbf{f}'_n dS'$ are not singular and can be evaluated analytically or numerically. The above

prescription is for flat tesselations, and along with the piecewise geometric description come challenges in accurately describing the physics of scattering from objects with singular features, e.g., cones, finite wedges, etc. While these are well known challenges (and the DPIE is not immune to these as they arise from the geometry as opposed to the operator), one could use singular basis functions [47] or adaptive basis [45, 48] to partially overcome some of the bottlenecks.

ACKNOWLEDGMENT

This work was supported in part by the National Science Foundation under Grant No. CCF-1822932 and by the US Air Force Research Laboratory under contracts FA8650-19-F-1747 and FA8650-20-C-1132. This research used resources of Michigan State University's High Performance Computing Center (MSU HPCC).

REFERENCES

- A. Poggio and E. Miller, "Chapter 4 integral equation solutions of three-dimensional scattering problems," in *Computer Techniques for Electromagnetics*, ser. International Series of Monographs in Electrical Engineering, R. Mittra, Ed. Pergamon, 1973, pp. 159 – 264.
- [2] C. Müller, Electromagnetic Waves in a Homogeneous Medium. Berlin, Heidelberg: Springer Berlin Heidelberg, 1969.
- [3] E. Marx, "Integral equation for scattering by a dielectric," *IEEE Transactions on Antennas and Propagation*, vol. 32, no. 2, pp. 166–172, 1984.
- [4] A. Glisson, "An integral equation for electromagnetic scattering from homogeneous dielectric bodies," *IEEE Transactions on Antennas and Propagation*, vol. 32, no. 2, pp. 173–175, 1984.
- [5] P. Yla-Oijala and M. Taskinen, "Well-conditioned muller formulation for electromagnetic scattering by dielectric objects," *IEEE Transactions* on Antennas and Propagation, vol. 53, no. 10, pp. 3316–3323, 2005.
- [6] J. Li, D. Dault, N. Nair, and B. Shanker, "Analysis of scattering from complex dielectric objects using the generalized method of moments," *JOSA A*, vol. 31, no. 11, pp. 2346–2355, 2014.
- [7] K. Cools, F. P. Andriulli, F. Olyslager, and E. Michielssen, "Time domain calderÓn identities and their application to the integral equation analysis of scattering by pec objects part i: Preconditioning," *IEEE Transactions* on Antennas and Propagation, vol. 57, no. 8, pp. 2352–2364, 2009.
- [8] G. Vecchi, "Loop-star decomposition of basis functions in the discretization of the efie," *IEEE Transactions on Antennas and Propagation*, vol. 47, no. 2, pp. 339–346, 1999.
- [9] Z. G. Qian and W. C. Chew, "A quantitative study on the low frequency breakdown of efie," *Microwave and Optical Technology Letters*, vol. 50, no. 5, pp. 1159–1162, 2008.
- [10] K. Cools, F. P. Andriulli, F. Olyslager, and E. Michielssen, "Nullspaces of mfie and calderÓn preconditioned efie operators applied to toroidal surfaces," *IEEE Transactions on Antennas and Propagation*, vol. 57, no. 10, pp. 3205–3215, 2009.
- [11] R. Kress and G. F. Roach, "Transmission problems for the helmholtz equation," *Journal of Mathematical Physics*, vol. 19, no. 6, pp. 1433–1437, 1978.
- [12] M. Costabel and E. P. Stephan, "Strongly elliptic boundary integral equations for electromagnetic transmission problems," *Proceedings of* the Royal Society of Edinburgh: Section A Mathematics, vol. 109, no. 3-4, p. 271–296, 1988.
- [13] P. Wilde, "Transmission problems for the vector helmholtz equation," Proceedings of the Royal Society of Edinburgh: Section A Mathematics, vol. 105, no. 1, p. 61–76, 1987.
- [14] M. Costabel, "A coercive bilinear form for maxwell's equations," *Journal of Mathematical Analysis and Applications*, vol. 157, no. 2, pp. 527–541, 1991.
- [15] A. Dely, "Computational strategies for impedance boundary condition integral equations in frequency and time domains," Ph.D. dissertation, Ecole nationale supérieure Mines-Télécom Atlantique, 2020.
- [16] D. R. Wilton and A. W. Glisson, "On improving the electric field integral equation at low frequencies," in *URSI National Radio Science Meeting Digest*, 1981, p. 24.

- [17] W. Wu, A. W. Glisson, and D. Kajfez, "A study of two numerial solution procedures for the electric field integral equation at low frequency," *Applied Computational Electromagnetics Society Journal*, vol. 10, no. 3, pp. 69–80, 1995.
- [18] M. Burton and S. Kashyap, "A study of a recent moment method algorithm that is accurate to very low frequencies," *Applied Computational Electromagnetics Society Journal*, vol. 10, no. 3, pp. 58–68, 1995.
- [19] F. P. Andriulli, K. Cools, I. Bogaert, and E. Michielssen, "On a well-conditioned electric field integral operator for multiply connected geometries," *IEEE Transactions on Antennas and Propagation*, vol. 61, no. 4, pp. 2077–2087, 2013.
- [20] C. L. Epstein and L. Greengard, "Debye sources and the numerical solution of the time harmonic maxwell equations," *Communications on Pure and Applied Mathematics*, vol. 63, no. 4, pp. 413–463, 2010.
- [21] X. Fu, J. Li, L. J. Jiang, and B. Shanker, "Generalized debye sources-based effe solver on subdivision surfaces," *IEEE Transactions on Antennas and Propagation*, vol. 65, no. 10, pp. 5376–5386, 2017.
- [22] W. C. Chew, "Vector potential electromagnetics with generalized gauge for inhomogeneous media: Formulation," *Progress In Electromagnetics Research*, vol. 149, pp. 69–84, January 2014.
- [23] Q. S. Liu, S. Sun, and W. C. Chew, "An integral equation method based on vector and scalar potential formulations," in 2015 IEEE International Symposium on Antennas and Propagation USNC/URSI National Radio Science Meeting, July 2015, pp. 744–745.
- [24] F. Vico, M. Ferrando, L. Greengard, and Z. Gimbutas, "The decoupled potential integral equation for time-harmonic electromagnetic scattering," *Communications on Pure and Applied Mathematics*, vol. 69, no. 4, pp. 771–812, 2016.
- [25] J. Li, X. Fu, and B. Shanker, "Potential integral equations in electromagnetics," in 2017 IEEE International Symposium on Antennas and Propagation USNC/URSI National Radio Science Meeting, July 2017.
- [26] F. Vico, L. Greengard, and M. Ferrando, "Decoupled field integral equations for electromagnetic scattering from homogeneous penetrable obstacles," *Communications in Partial Differential Equations*, vol. 43, no. 2, pp. 159–184, 2018.
- [27] J. Helsing, A. Karlsson, and A. Rosén, "Comparison of integral equations for the maxwell transmission problem with general permittivities," 2020.
- [28] F. Vico, M. Ferrando-Bataller, T. B. Jiménez, and A. Berenguer, "A high order locally corrected nyström implementation of the decoupled potential integral equation," in 2015 9th European Conference on Antennas and Propagation (EuCAP), 2015, pp. 1–4.
- [29] T. E. Roth and W. C. Chew, "Development of stable A-φ time-domain integral equations for multiscale electromagnetics," *IEEE Journal on Multiscale and Multiphysics Computational Techniques*, vol. 3, pp. 255–265, 2018.
- [30] T. E. Roth and W. C. Chew, "Radiation gauge potential-based time domain integral equations for penetrable regions," *Progress In Electro*magnetics Research, vol. 168, pp. 73–86, 2020.
- [31] Z. Qian and W. C. Chew, "Fast full-wave surface integral equation solver for multiscale structure modeling," *IEEE Transactions on Antennas and Propagation*, vol. 57, no. 11, pp. 3594–3601, 2009.
- [32] J. Li, X. Fu, and B. Shanker, "Decoupled potential integral equations for electromagnetic scattering from dielectric objects," *IEEE Transactions* on Antennas and Propagation, vol. 67, no. 3, pp. 1729–1739, March 2019.
- [33] S. Rao, D. Wilton, and A. Glisson, "Electromagnetic scattering by surfaces of arbitrary shape," *IEEE Transactions on Antennas and Prop*agation, vol. 30, no. 3, pp. 409–418, May 1982.
- [34] D. Tihon and C. Craeye, "All-analytical evaluation of the singular integrals involved in the method of moments," *IEEE Transactions on Antennas and Propagation*, vol. 66, no. 4, pp. 1925–1936, 2018.
- [35] D. Dault and B. Shanker, "An interior penalty method for the generalized method of moments," *IEEE Transactions on Antennas and Propagation*, vol. 63, no. 8, pp. 3561–3568, 2015.
- [36] J. Yuan and B. Shanker, "Analysis of the spectrum of the single integral equation for scattering from dielectric objects," in 2005 IEEE Antennas and Propagation Society International Symposium, vol. 2B, 2005, pp. 93–96 vol. 2B.
- [37] G. C. Hsiao and R. E. Kleinman, "Mathematical foundations for error estimation in numerical solutions of integral equations in electromagnetics," *IEEE Transactions on Antennas and Propagation*, vol. 45, no. 3, pp. 316–328, 1997.
- [38] S. Yan, J. Jin, and Z. Nie, "Calderón preconditioner: From efie and mfie to n-müller equations," *IEEE Transactions on Antennas and Propaga*tion, vol. 58, no. 12, pp. 4105–4110, 2010.

- [39] J. A. Stratton, Spherical Waves. John Wiley & Sons, Ltd, 2015, ch. VII, pp. 392–423.
- [40] D. Wilton, S. Rao, A. Glisson, D. Schaubert, O. Al-Bundak, and C. Butler, "Potential integrals for uniform and linear source distributions on polygonal and polyhedral domains," *IEEE Transactions on Antennas* and Propagation, vol. 32, no. 3, pp. 276–281, 1984.
- [41] R. E. Hodges and Y. Rahmat-Samii, "The evaluation of mfie integrals with the use of vector triangle basis functions," *Microwave and Optical Technology Letters*, vol. 14, no. 1, pp. 9–14, 1997.
- [42] P. W. Fink, D. R. Wilton, and M. A. Khayat, "Simple and efficient numerical evaluation of near-hypersingular integrals," *IEEE Antennas* and Wireless Propagation Letters, vol. 7, pp. 469–472, 2008.
- [43] M. M. Botha, "A family of augmented duffy transformations for nearsingularity cancellation quadrature," *IEEE Transactions on Antennas and Propagation*, vol. 61, no. 6, pp. 3123–3134, 2013.
- [44] A. Alsnayyan, J. Li, S. Hughey, A. Diaz, and B. Shanker, "Efficient isogeometric boundary element method for analysis of acoustic scattering from rigid bodies," *The Journal of the Acoustical Society of America*, vol. 147, no. 5, pp. 3275–3284, 2020.
- [45] D. Dault and B. Shanker, "A mixed potential mlfma for higher order moment methods with application to the generalized method of moments," *IEEE Transactions on Antennas and Propagation*, vol. 64, no. 2, pp. 650–662, 2015.
- [46] T. Terai, "On calculation of sound fields around three dimensional objects by integral equation methods," *Journal of Sound and Vibration*, vol. 69, no. 1, pp. 71 100, 1980.
- [47] R. D. Graglia, A. F. Peterson, and L. Matekovits, "Singular, hierarchical scalar basis functions for triangular cells," *IEEE Transactions on Antennas and Propagation*, vol. 61, no. 7, pp. 3674–3692, 2013.
- [48] N. V. Nair and B. Shanker, "Generalized method of moments: A novel discretization technique for integral equations," *IEEE transactions on antennas and propagation*, vol. 59, no. 6, pp. 2280–2293, 2011.



Charles A. Macon (S'92-M'01-SM'10) received the B.S., M.S., and Ph.D. degrees in electrical engineering from Michigan State University, East Lansing, MI, USA in 1993, 1998, and 2001, respectively. From 1993 to 1997, he was a Power Systems Engineer with Consumers Energy Company, Grand Rapids, MI, USA. From 1999 to 2001, he was a Research Assistant with the Electromagnetics Research Group, Michigan State University. In 2002, he joined High Performance Technologies, Inc. (acquired by SAIC in 2019), Reston, VA, USA, as a Computa-

tional Scientist. He was their computational electromagnetics research contract lead with the Army Research Laboratory, Aberdeen, MD, USA, under the Department of Defense High Performance Computing Modernization Program. In 2004, he joined the Air Force Research Laboratory (AFRL), Wright-Patterson Air Force Base (WPAFB), OH, USA, as an Electromics Engineer. He led numerous research projects to improve national computational electromagnetics, antenna modeling, and RF measurement capabilities. From 2006-2008, while at AFRL, he was an Adjunct Assistant Professor at the Air Force Institute of Technology, WPAFB, OH, USA, where he taught computational electromagnetics and advised students. He is currently a Principal Electronics Engineer where he oversees and conducts electromagnetics-related research and development. His research interests include computational electromagnetics, high performance computing, antenna modeling, radar, and RF measurements.



Luke Baumann (S'14) received the B.S. degree in computer engineering from California Polytechnic State University, San Luis Obsipo, CA in 2014 and the M.S. degree in electrical engineering from Michigan State University in 2021 where he is currently a Ph.D. candidate. His research interests include well-conditioned formulations, surface integral equation methods, and fast algorithms in electromagnetics.



H. M. Aktulga is an Associate Professor in the Department of Computer Science and Engineering at Michigan State University (MSU) where he directs the Scalable Parallel Technologies and Algorithms (SParTA) group. He primarily works on the design and development of parallel algorithms, numerical methods, performance models and software systems to harness the full potential of state-of-the-art HPC platforms for challenging problems in large scale scientific computing and big-data analytics. A distinguishing aspect of his research is the close

collaborations that he has built with domain experts in a wide range of fields such as molecular modeling and simulation, materials science, computational electromagnetics, and nuclear physics. The SParTA group is a contributor to AMBER and LAMMPS software, which are widely used packages for molecular dynamics. Dr. Aktulga has been an author/co-author in over 50 research articles in prestigious journals, conferences and book series. He is a recipient of the 2019 NSF CAREER award.



B. Shanker received his B'Tech from the Indian Institute of Technology, Madras, India in 1989, M.S. and Ph.D in 1992 and 1993, respectively, from the Pennsylvania State University. From 1993 to 1996 he was a research associate in the Department of Biochemistry and Biophysics at Iowa State University where he worked on the Molecular Theory of Optical Activity. From 1996 to 1999 he was with the Center for Computational Electromagnetics at the University of Illinois at Urbana-Champaign as a Visiting Assistant Professor, and from 1999-

2002 with the Department of Electrical and Computer Engineering at Iowa State University as an Assistant Professor. Currently, he is a University Distinguished Professor (an honor accorded to about 2% of MSU faculty members) in the Department of Electrical and Computer Engineering at Michigan State University, and the Department of Physics and Astronomy. From 2015-2018, he was appointed Associate Chair of the Department of Computational Mathematics, Science and Engineering, a new department at MSU and was a key player in building this Department. Earlier he served as the Associate Chair for Graduate Studies in the Department of Electrical and Computer Engineering from 2012-2015, and currently is the Associate Chair for Research in ECE. He has authored/co-authored around 450 journal and conference papers and presented a number of invited talks. His research interests include all aspects of computational electromagnetics (frequency and time domain integral equation based methods, multi-scale fast multipole methods, fast transient methods, higher order finite element and integral equation methods), propagation in complex media, mesoscale electromagnetics, and particle and molecular dynamics as applied to multiphysics and multiscale problems. He was an Associate Editor for IEEE Antennas and Wireless Propagation Letters (AWPL) and IEEE Transactions on Antennas and Propagation, was the Topical Editor for Journal of Optical Society of America: A, and is a full member of the USNC-URSI Commission B. He is Fellow of IEEE, elected for his contributions in computational electromagnetics. He has also been awarded the Withrow Distinguished Junior scholar (in 2003), Withrow Distinguished Senior scholar (in 2010), the Withrow teaching award (in 2007), and the Beal Outstanding Faculty award (2014).